

DTIC FILE COPY

②

Applied Research Laboratory

AD-A228 490

Technical Report

DTIC
ELECTE
NOV 14 1990
S E D
C3

PENNSTATE



DISTRIBUTION STATEMENT A	
Approved for public release; Distribution Unlimited	

The Pennsylvania State University
APPLIED RESEARCH LABORATORY
P.O. Box 30
State College, PA 16804

THE MODIFICATION OF BACKGROUND
DENSITY PROFILES IN THERMOHALINE CONVECTION

by

J. L. Schramm
H. N. Shirer
R. Wells

Technical Report No. TR 90-014
November 1990

DTIC
FLECTE
NOV 14 1990
E D

Supported by:
Space and Naval Warfare Systems Command

L.R. Hettche, Director
Applied Research Laboratory

Approved for public release; distribution unlimited

90 11 13 149

REPORT DOCUMENTATION PAGE

Form Approved
OMB No. 0704-0188

Public reporting burden for the collection of information is estimated to average 1 hour per response, including the time for reviewing instructions, searching existing data sources, gathering and maintaining the data needed, and completing and reviewing the collection of information. Send comments regarding this burden estimate or any other aspect of this collection of information, including suggestions for reducing this burden, to Washington Headquarters Services, Directorate for Information Operations and Reports, 1215 Jefferson Davis Highway, Suite 1204, Arlington, VA 22202-4302, and to the Office of Management and Budget, Paperwork Reduction Project 0704-0188, Washington, DC 20503.

1. AGENCY USE ONLY (Leave blank)	2. REPORT DATE	3. REPORT TYPE AND DATES COVERED	
	November 1990		
4. TITLE AND SUBTITLE		5. FUNDING NUMBERS	
THE MODIFICATION OF BACKGROUND DENSITY PROFILES IN THERMOHALINE CONVECTION			
6. AUTHOR(S)			
J. L. Schramm, H. N. Shirer, R. Wells			
7. PERFORMING ORGANIZATION NAME(S) AND ADDRESS(ES)		8. PERFORMING ORGANIZATION REPORT NUMBER	
Applied Research Laboratory The Pennsylvania State University P. O. Box 30 State College, PA 16804		TR# 90-014	
9. SPONSORING/MONITORING AGENCY NAME(S) AND ADDRESS(ES)		10. SPONSORING/MONITORING AGENCY REPORT NUMBER	
Space and Naval Warfare Systems Command Department of the Navy Washington, DC 20363-5100		N000039-88-C-0051	
11. SUPPLEMENTARY NOTES			
12a. DISTRIBUTION/AVAILABILITY STATEMENT		12b. DISTRIBUTION CODE	
Unlimited			
13. ABSTRACT (Maximum 200 words)			
<p>Density profile modification in thermohaline convection is examined with a sixteen-coefficient spectral model derived from the two-dimensional, shallow Boussinesq equations. These density modifications are important in near-neutral density stratifications because they can significantly alter the depth and location of the near-surface sound channel. in the ocean. A linear stability analysis of the conductive solution gives a characteristic equation from which the Hopf bifurcation points signalling the onset of convective, or temporally periodic, solutions can be determined. Two horizontal wavenumbers are included to allow the existence of a double Hopf point, which when separated, may yield diffeo-Hopf points on the periodic solutions and so allow for secondary branching, or toral, solutions. The periodic solutions associated with the Hopf bifurcations are the toral solutions associated with the diffeo-Hopf points are then studied.</p>			
<p>An example using parameter values corresponding to those of melting sea ice is presented. In this case, the toral solutions are always unstable owing to the existence of a diffeo-Hopf point exclusively on the unstable periodic solution that branches second from the conductive solution. Thus, the competition between the stabilizing salinity gradient and destabilizing</p>			
14. SUBJECT TERMS		(continued on next page)	
density profiles, thermohaline convection, Boussinesq equation, Hopf point, melting sea ice		15. NUMBER OF PAGES	
		16. PRICE CODE	
17. SECURITY CLASSIFICATION OF REPORT	18. SECURITY CLASSIFICATION OF THIS PAGE	19. SECURITY CLASSIFICATION OF ABSTRACT	20. LIMITATION OF ABSTRACT
Unclassified	Unclassified	Unclassified	SAR

THE MODIFICATION OF BACKGROUND DENSITY PROFILES IN THERMOHALINE CONVECTION
Abstract (continued)

temperature gradient allows only stable steady and stable periodic solutions, and it is these solutions that modify the background density profiles. The periodic solutions are characterized by an unstable density profile moving alternately between the interior and the boundaries. Hence, the sound channel alternately increases and decreases in depth and in location relative to the surface. In contrast, the steady solutions produce an unstable density gradient in the interior of the domain. Thus, in the steady case, there is always a near-surface sound channel.

Accession For

DIS GRA&I
IC TAB
Unannounced
Justification

by _____

Distribution/

Availability Codes
Mail and/or
Fist Special

A-1

ABSTRACT

Density profile modification in thermohaline convection is examined with a sixteen-coefficient spectral model derived from the two-dimensional, shallow Boussinesq equations. These density modifications are important in near-neutral density stratifications because they can significantly alter the depth and location of the near-surface sound channel in the ocean. A linear stability analysis of the conductive solution gives a characteristic equation from which the Hopf bifurcation points signalling the onset of convective, or temporally periodic, solutions can be determined. Two horizontal wavenumbers are included to allow the existence of a double Hopf point, which when separated, may yield diffeo-Hopf points on the periodic solutions and so allow for secondary branching, or toral, solutions. The periodic solutions associated with the Hopf bifurcations and the toral solutions associated with the diffeo-Hopf points are then studied.

An example using parameter values corresponding to those of melting sea ice is presented. In this case, the toral solutions are always unstable owing to the existence of a diffeo-Hopf point exclusively on the unstable periodic solution that branches second from the conductive solution. Thus, the competition between the stabilizing salinity gradient and destabilizing temperature gradient

allows only stable steady and stable periodic solutions, and it is these solutions that modify the background density profiles. The periodic solutions are characterized by an unstable density profile moving alternately between the interior and the boundaries. Hence, the sound channel alternately increases and decreases in depth and in location relative to the surface. In contrast, the steady solutions produce an unstable density gradient in the interior of the domain. Thus, in the steady case, there is always a near-surface sound channel.

TABLE OF CONTENTS

	<u>Page</u>
LIST OF TABLES	vii
LIST OF FIGURES	viii
LIST OF SYMBOLS	xi
ACKNOWLEDGMENTS	xvii
Chapter 1 INTRODUCTION	1
Chapter 2 MODEL DEVELOPMENT	9
2.1 The Boussinesq Equations and Boundary Conditions . .	10
2.2 Dimensionless Forms	14
2.3 Linear Stability Analysis	16
2.4 The Spectral Model	30
Chapter 3 FINDING BIFURCATION POINTS ON PERIODIC SOLUTIONS . .	38
3.1 Stability of a Periodic Solution	38
3.2 Eigenvalue Calculation and Analysis	41
3.2.1 Subharmonic Bifurcation	48
3.2.2 Harmonic Bifurcation	49
3.2.3 Toral Bifurcation	49
Chapter 4 PHYSICAL INTERPRETATION OF MODEL SOLUTIONS	51
4.1 Bifurcation Diagrams Representing Model Solutions .	51
4.2 Physical Interpretation of the Periodic and Steady Solutions	68
4.2.1 Thermohaline Convection in Estuaries	69

TABLE OF CONTENTS (continued)

	<u>Page</u>
4.2.2 Thermohaline Convection Under Melting Sea Ice	71
Chapter 5 CONCLUSION	91
REFERENCES	98

LIST OF TABLES

<u>Table</u>	<u>Page</u>
1 Estimates of the five largest eigenvalues μ_i for $Ra_S=5.0$, $Ra_T=12.8$, $H_m=12.25$, $a=0.486$, $m=2$, and $j=1$ for different timesteps Δt and iterates N in the integration	46
2 Typical values of horizontal and vertical eddy diffusion coefficients for large-scale motion of sea water (after Apel, 1987)	73

LIST OF FIGURES

<u>Figure</u>	<u>Page</u>
1 The dependence of the Hopf bifurcation points H_m and H_j on the aspect ratio where $Ra_S=65$, $m=2$, $j=1$, $P=7$, and $\tau=0.01$	21
2 Convective regimes in the inviscid case where positive values of Ra_T and Ra_S represent destabilizing and stabilizing gradients, respectively	24
3 Convective (unshaded) and conductive (shaded) when there are diffusion and viscosity	25
4 Schematic depiction of the convective (periodic), salt finger, and conductive regimes	26
5 Schematic depiction of the motion of parcels in the stable conductive and periodic regimes	28
6 Schematic bifurcation diagrams showing (a) periodic and toral and (b) steady solutions of horizontal wavenumbers m and j	32
7 Bifurcation diagram for $Ra_S=1.6836$, $a=0.486$, $m=2$, $j=1$, $P=7$, and $\tau=0.01$	53
8 Bifurcation diagram for $Ra_S=5.0$, $a=0.486$, $m=2$, $j=1$, $P=7$, and $\tau=0.01$	54
9 A schematic depiction of the periodic branch P_m in (a) the five-coefficient model and in (b) the sixteen-coefficient model	59
10 Variation of the values of the bifurcation points with aspect ratio when $Ra_S=1.6836$, $m=2$, $j=1$, $P=7$, and $\tau=0.01$	62
11 Variation of the values of the bifurcation points with aspect ratio when $Ra_S=5.0$, $m=2$, $j=1$, $P=7$, and $\tau=0.01$	64

LIST OF FIGURES (continued)

<u>Figure</u>	<u>Page</u>
12 Bifurcation diagram for $Ra_S=65$, $a=0.486$, $m=2$, $j=1$, $P=7$, and $\tau=0.01$	65
13 Background profiles (lines) and modification of the background profiles (curves) for salinity (a), temperature (b), and density (c) as functions of depth when $Ra_S=1.6836$, $Ra_T=9.7$, $a=0.486$, $m=2$, $j=1$, $P=7$, and $\tau=0.01$ for steady solution S_m	67
14 Winter distributions of salinity (a) and temperature (b) in a longitudinal section of Hardangerfjord, Norway (from Dyer, 1973)	70
15 Schematic temperature distributions with depth for tropical (a), mid-latitude (b), and polar regions (c) for summer (solid) and winter (dashed) conditions . . .	72
16 Values of domain depth z_T (m) for the double Hopf point with the following values: $K_T=14.286 \text{ m}^2/\text{s}$, $\nu=100 \text{ m}^2/\text{s}$, $P=7$, $T_{00}=283 \text{ K}$, $S_{00} 35\%$, $\Delta T=6 \text{ K}$, $\Delta S=0.742\%$, $m=2$, $j=1$, $g=9.8 \text{ m}^2/\text{s}$, and $a_{mj}=0.49343$	75
17 Variations in salinity coefficients S_{m1} and S_{02} , temperature coefficients T_{m1} and T_{02} , and stream function coefficient ψ_{m1} for the periodic solution P_m in the Veronis model for values of $Ra_S=65$, $Ra_T=64.94$, $a=0.486$, $P=7$, $\tau=0.01$, and $m=2$	76
18 Variations in density coefficients ρ_{02} and ρ_{m1} and stream function coefficient ψ_{m1} corresponding to the periodic solution in Figure 17	78

LIST OF FIGURES (continued)

<u>Figure</u>	<u>Page</u>
19 Contours of convective density ρ'_c (kg/m ³), stream function ψ'_c (m ² /s), and the modification of the background density ρ'_b (kg/m ³) for the periodic solution in Figure 18 (x and z are dimensionless)	80
20 Contours of convective density ρ'_c (kg/m ³), stream function ψ'_c (m ² /s), and the modification of the background density ρ'_b (kg/m ³) for the steady solution S_m with the values $Ra_S=65$, $Ra_T=65.1$, $K_f=14.286$ m ² /s, $\nu=100$ m ² /s, $P=7$, $T_{00}=283$ K, $S_{00}=35\%$., $\Delta T=6$ K, $\Delta S=0.742\%$., $m=2$, $j=1$, $g=9.8$ m/s ² , $a_{mj}=0.49343$, and $\tau=0.01$	89

LIST OF SYMBOLS

a	domain aspect ratio
a_{mj}	domain aspect ratio at P_{mj}
B	16x16 matrix
C	5x5 matrix from V_k
\underline{c}	5 component vector of V_k related to C
D	9x9 matrix
\underline{d}	5 component vector related to D
D_j	value of Ra_T at the diffeo-Hopf point on P_j
D_m	value of Ra_T at the diffeo-Hopf point on P_m
F_j	value of Ra_T at the steady regular turning point on S_j
F_m	value of Ra_T at the steady regular turning point on S_m
g	acceleration due to gravity
G_{j5}	value of Ra_T at the periodic regular turning point on P_j in V_j
G_{m5}	value of Ra_T at the periodic regular turning point on P_m in V_m
G_{j9}	value of Ra_T at the harmonic bifurcation point on P_j
G_{m9}	value of Ra_T at the harmonic bifurcation point on P_m
H_j	value of Ra_T at the Hopf bifurcation point for horizontal wavenumber j and a given Ra_S

LIST OF SYMBOLS (continued)

H_k	value of Ra_T at the Hopf bifurcation point for horizontal wavenumber k and a given Ra_S
H_m	value of Ra_T at the Hopf bifurcation point for horizontal wavenumber m and a given Ra_S
H_{mj}	value of Ra_T at the double Hopf bifurcation point for horizontal wavenumber m and j
j	horizontal integral wavenumber
J	Jacobian operator
k	horizontal integral wavenumber
\hat{k}	unit vector in the z -direction
K_S	solutal diffusivity
K_T	thermal diffusivity
L	characteristic length in the x -direction
m	horizontal integral wavenumber
n	vertical integral wavenumber
N	number of integrations
p	pressure
p_0	pressure of conductive state
p'	pressure perturbation due to convection
P	Prandtl number
P_j	periodic solution of horizontal wavenumber j

LIST OF SYMBOLS (continued)

P_m	periodic solution of horizontal wavenumber m
P_{m+j}	periodic solution of horizontal wavenumber $m+j$
P_{m-j}	periodic solution of horizontal wavenumber $m-j$
Ra_S	solutal Rayleigh number
Ra_T	thermal Rayleigh number
Ra_{Tc}	critical thermal Rayleigh number
Ra_{Tmin}	minimum value of Ra_T for the development of convection
S	32-equation system
S	salinity
S_0	salinity of conductive state
S_{00}	salinity at bottom of domain
S'	salinity perturbation (convection)
S'_b	modification to background salinity by convection
S'_c	perturbation salinity in convective state
S_j	steady solution of horizontal wavenumber j
S_m	steady solution of horizontal wavenumber m
t	time
T	period
T_a	approximate period

LIST OF SYMBOLS (continued)

T	temperature
T_0	temperature of conductive state
T_{00}	temperature at bottom of domain
T'	temperature perturbation (convection)
T'_b	modification to background temperature by convection
T'_c	perturbation temperature in convective state
u'	horizontal component of velocity due to convection
v'	perturbation velocity
v_j	Veronis five-coefficient model of wavenumber j
v_m	Veronis five-coefficient model of wavenumber m
w'	vertical component of velocity due to convection
x	horizontal distance
x_i	perturbations in the direction i
y	independent variable
z	height
z_T	fluid depth
α	thermal expansion coefficient
β	solutal expansion coefficient
ΔS	vertical salinity difference

LIST OF SYMBOLS (continued)

β	solutal expansion coefficient
ΔS	vertical salinity difference
ΔT	vertical temperature difference
Δt	timestep
λ	complex root to polynomial equation
μ	eigenvalue or characteristic multiplier
ν	kinematic viscosity
ξ	constant where $\xi = a^2 k^2 + n^2$
π	$\pi = 3.1415926\dots$
ρ	density
ρ_0	density of conductive state
ρ_{00}	density at bottom of domain
ρ'	density perturbation (convection)
ρ_b'	modification to background density by convection
ρ_c'	perturbation density in convective state
ρ_e	density of the environment
ρ_p	density of a parcel
τ	ratio of diffusivities
ψ	stream function
ψ_c	stream function due to convection

LIST OF SYMBOLS (continued)

$\frac{\partial}{\partial t}(\cdot)$ local derivative

$\nabla(\cdot)$ gradient

$\nabla^2(\cdot)$ Laplacian

$\tilde{\nabla}^2(\cdot)$ dimensionless Laplacian

(\cdot)^{*} dimensionless variable

Chapter 1

INTRODUCTION

Acoustic waves constitute one important mode in the dynamics of the ocean. Propagation of these waves is greatly affected by the salinity and temperature fields; the vertical profiles of salinity and temperature support such density-driven processes as thermohaline convection, salt-fingering, and small-scale mixing. Density differences caused by these processes may lead to the development of a near-surface sound channel that traps acoustical energy and allows it to propagate over large distances (Apel, 1987). By understanding the background density profiles that characterize these phenomena, we can gain insight into how acoustic waves propagate in the vicinity of these density variations.

Focusing on thermohaline convection, we consider a fluid in which both the temperature and salt concentration decrease linearly with height. This configuration may be observed in estuaries or near melting sea ice. In thermohaline convection, the two components, heat and salinity, act in opposite ways to alter the vertical density gradient. Heating from below or cooling from above acts to destabilize the fluid by causing the density of the fluid at the bottom to decrease or at the top to increase to values sufficient for convective overturning to occur. Freshening above or salting below

acts to increase the density at the bottom of the fluid, thereby stabilizing the system.

We can further understand the physical mechanisms of thermohaline convection by using a parcel argument (Huppert and Moore, 1976). If a parcel is initially raised from its equilibrium position in a fluid having decreasing temperature and salinity gradients, then it comes into an environment that is cooler and less salty. Because temperature diffuses much more rapidly than salt, the parcel quickly equilibrates to the temperature of its environment, making the parcel saltier and more dense than its surroundings. The parcel sinks, overshooting its initial position. The temperature again equilibrates rapidly with that of the environment, and so the parcel becomes fresher than its surroundings. It is therefore less dense, rises toward its initial position, which it again overshoots. An oscillatory response occurs that can be either (i) damped, or (ii) periodic, depending on how fresh the parcel is as compared with its environment. If the gradients driving the motion are small, then the parcel is only slightly fresher than its environment, and so it cannot rise to its initial height. Thus, the result is a damped oscillation to its equilibrium position. In the other case, the parcel is much fresher than its environment, it returns to its initial position and a stable oscillation occurs. Based on the

conservation of mass, vertical motion in a system bounded above and below will lead to divergence in the horizontal; this allows the existence of two-dimensional convective cells.

The above behavior can be expressed mathematically in the following way. For a given salinity gradient, which can be represented by a salinity Rayleigh number Ra_S , a periodic solution replaces the conductive state when the temperature gradient, represented by a thermal Rayleigh number Ra_T , exceeds a critical value H_k . This critical value is known as a Hopf bifurcation point from which emanates a periodic, or convective, solution characterized by single horizontal and vertical wavenumbers. This periodic solution is only one of the infinite number of branching solutions represented by the governing equations of motion. The wavenumber of the periodic solution that bifurcates first is the preferred one that is expected to be observed in the fluid (Laufersweiler, 1987). Veronis (1965) found steady and periodic solutions in thermohaline convection using a model consisting of five coupled, nonlinear ordinary differential equations. In the Veronis model, the value of Ra_T at the Hopf bifurcation point is much less than the value of Ra_T at the steady bifurcation point. This result is a manifestation of the slow diffusivity of salt. In this model, the convective flow and

its distortions of the mean temperature, salinity, and velocity fields are minimally represented.

Using the Veronis (1965) system of equations with moderate values of Ra_S , Da Costa et al. (1981), Knobloch and Proctor (1981), and Knobloch et al. (1986) found oscillatory solutions ending on unstable steady branches as the thermal forcing rate was increased. For large values of Ra_S , they found a period doubling cascade to a chaotic solution as the magnitude of Ra_T was increased. This is one of the many routes to chaos that have been proposed (e.g. Nese, 1987).

For rotating Rayleigh-Bénard convection, Wells and Shirer (1987) found quasi-periodic, or toral solutions that involve the nonlinear coupling of two separate circulations dominated by two horizontal wavenumbers. These results were obtained using a spectral model that contained a double Hopf point, at which coincide two Hopf bifurcation points characterizing periodic solutions of two different horizontal wavenumbers. Although modification of the background state was not examined for the toral case, the model of Wells and Shirer (1987) did provide an explanation of cell broadening and period shortening in rotating convection. Noting that thermohaline convection also has double Hopf points, we investigate whether the same wavenumber

changing mechanism associated with toral solutions exists in thermohaline convection.

Beginning with the two-dimensional, shallow Boussinesq system, we convert the partial differential equations to a dimensionless form that allows us to define Ra_S and Ra_T as well as the other dimensionless parameters. A linear stability analysis is then performed on the conductive solution to these equations to determine the characteristic equation from which we can deduce the bifurcation points signalling the occurrence of convective solutions. From this analysis, we can find the preferred horizontal wavenumber, the values of Ra_T for the steady and Hopf bifurcations, and the value of the aspect ratio a and the magnitude of Ra_T at the double Hopf point. To find approximations of the solutions branching from the conductive solution at Hopf bifurcation points, we develop a nonlinear spectral model.

We need expansions for the salinity, temperature, and velocity fields that are solutions to the linearized equations of motion and that satisfy the cyclic, stress-free boundary conditions for flow in a rectangular domain. Here, trigonometric functions suffice. To capture the solution at the double Hopf point, we must include at least two horizontal wavenumbers, m and j , and vertical wavenumber one in the representations of the dependent variables. We may think

of a double Hopf point as the superposition of two simple Hopf points; when these two Hopf points are separated, a toral or secondary branching solution may occur at a diffeo-Hopf point. Based on the results of Chang and Shirer (1984) and Wells and Shirer (1987), we find that representation of this solution requires catalytic components having horizontal wavenumbers $m+j$ and $m-j$, and vertical wavenumber two. These catalytic terms represent a transfer of stability from a solution having one horizontal wavenumber to one having another. The wavenumber sets $(m,1)$, $(j,1)$, $(m+j,2)$, and $(m-j,2)$ are only four of the infinite number of sets involved in solutions to the partial differential equations.

To represent the changes in the mean background salinity and temperature fields by the convective flow, several more terms in the variable expansions are needed (Veronis, 1968). The interaction between the $(m,1)$ modes, or the $(j,1)$ modes can be represented by components having horizontal wavenumber zero and vertical wavenumber two. To account for the modification of the background profiles by toral solutions, we add temperature and salinity coefficients for horizontal and vertical wavenumbers zero and four, respectively. These $(0,2)$ and $(0,4)$ terms represent the attempt by the circulation to eliminate an unstable density gradient. Summing the terms in the expansions gives a total of sixteen trigonometric functions needed to

represent toral convective solutions and the modifications of the background density field by these solutions.

Using this sixteen-coefficient low-order spectral model, which is composed of two nonlinearly linked Veronis models representing periodic solutions having horizontal wavenumbers m and j , we will examine the development of quasi-periodic solutions. We study this development in the following way. Noting that the occurrence of a diffeo-Hopf point is related to the separation of the double Hopf point whose value depends on the aspect ratio a , we choose a value of a near that of the double Hopf point and then increase the value of Ra_T past that for the first Hopf bifurcation point. The resulting stable, periodic solution is characterized by either wavenumber m or j , and we increase the value of Ra_T further until a diffeo-Hopf bifurcation occurs on this periodic solution. This diffeo-Hopf bifurcation point can be found using a stability analysis of the periodic solution. At the diffeo-Hopf bifurcation, temporal behavior is excited in the catalytic terms, and so a quasi-periodic or toral solution becomes possible. We are interested in the thermohaline circulations that correspond to these toral solutions and also in the way these quasi-periodic solutions modify the background density profiles (Veronis, 1968).

We begin in the following chapter by developing the model. In

Chapter 3, we construct a system of perturbation equations that will be used to determine the stability of the periodic solutions. This examination of stability will allow us to locate, via an eigenvalue analysis, the diffeo-Hopf bifurcations, as well as other ones -- harmonic bifurcations, and period doubling bifurcations -- on the periodic solutions. The results of this analysis and some examples of the circulations corresponding to steady and periodic solutions are examined in Chapter 4. In these examples, parameter values corresponding to those characterizing various oceanic flows are used. Discussion focusing on the modification of the background density by these steady and periodic solutions is also included. Concluding remarks are found in Chapter 5.

Chapter 2

MODEL DEVELOPMENT

In double-diffusive convection, several types of motion are possible. The flow resulting from a particular mechanism depends on whether the driving energy comes from the substance of higher or lower diffusivity (Turner, 1973). In thermohaline convection, the diffusivity of temperature is 100 times that of salt. This large difference in diffusivities produces a destabilizing process that maintains convective motion in both the diffusive regime and the salt finger regime.

Here, we focus on the diffusive regime in which cold, fresh water overlies warm, salty water. This situation can be produced in a layer of fluid, for example, by heating and salting it from below. In this case, a stabilizing salinity gradient and a destabilizing temperature gradient are created.

The diffusive mode may occur at the mouths of rivers or near melting ice islands in the Arctic Ocean (Turner, 1973). Indeed, sea ice strongly influences the suppression or development of convection. For example, melting sea ice increases the static stability of a column by adding fresh water to the surface, while the formation of sea ice destabilizes the water column by introducing salt into the upper layer.

To study the circulation induced in the diffusive regime by the temperature and salinity gradients, we introduce the Boussinesq equations of motion. A linear stability analysis of the conductive state reveals some properties of flow in the diffusive regime. Finally, a Fourier series solution to these partial differential equations is assumed, and then truncated to produce a low-order spectral model, as shown in the final section.

2.1 The Boussinesq Equations and Boundary Conditions

In the Boussinesq system, variables can be expressed as sums of the conductive and convective elements:

$$\underline{v}(x, z, t) = \underline{v}'(x, z, t) , \quad (2.1)$$

$$\rho(x, z, t) = \rho_{00} + \rho_0(z) + \rho'(x, z, t) , \quad (2.2)$$

$$T(x, z, t) = T_0(z) + T'(x, z, t) , \quad (2.3)$$

$$S(x, z, t) = S_0(z) + S'(x, z, t) , \quad (2.4)$$

$$p(x, z, t) = p_0(z) + p'(x, z, t) , \quad (2.5)$$

where \underline{v} , ρ , T , S , and p are velocity, density, temperature, salinity, and pressure. The subscripts 0 and ∞ denote the conductive state and the primes denote the convective state. Here, we note that a three-variable density decomposition is used in (2.2) instead of the

usual two-variable one. Substituting (2.1)-(2.5) into the full governing thermohaline equations gives the motionless and conductive state. This conductive, motionless state is a hydrostatic, horizontal layer of fluid of depth z_T and density $\rho_{00} + \rho_0(z)$ and is characterized by a quadratic profile of pressure and by linear vertical profiles of density ρ_0 , temperature T_0 , and salinity S_0 ; these are given by

$$\frac{\partial p_0}{\partial z} = -g (\rho_0 + \rho_{00}) , \quad (2.6)$$

$$T_0 = T_{00} - z \Delta T / z_T , \quad (2.7)$$

$$S_0 = S_{00} - z \Delta S / z_T , \quad (2.8)$$

where ρ_{00} , p_{00} , T_{00} , and S_{00} are, respectively, the magnitudes of density, pressure, temperature, and salinity at $z = 0$. The vertical differences of S and T are given by ΔT and ΔS . In the diffusive regime, the values of ΔT and ΔS are both positive. The relationship between $\rho_0(z)$, $T_0(z)$, and $S_0(z)$ is given below.

Restricting motion to the two dimensions, x and z , we may follow Veronis (1965) and write the Boussinesq equations as

$$\frac{\partial v'}{\partial t} + \frac{\sim}{\sim} v' \cdot \frac{\nabla v'}{\sim} = \frac{-1}{\rho_{00}} \frac{\nabla p'}{\sim} - \frac{gk(\rho_0 + \rho')}{\rho_{00}} + \nu \frac{\nabla^2 v'}{\sim} , \quad (2.9)$$

$$\frac{\nabla \cdot v'}{\sim} = 0 . \quad (2.10)$$

The conservation equations for temperature and salinity are

$$\frac{\partial T'}{\partial t} + \mathbf{v}' \cdot \nabla T' - \frac{w' \Delta T}{z_T} = K_T \mathbf{v}^2 T' , \quad (2.11)$$

$$\frac{\partial S'}{\partial t} + \mathbf{v}' \cdot \nabla S' - \frac{w' \Delta S}{z_T} = K_S \mathbf{v}^2 S' . \quad (2.12)$$

Here, the thermal and solutal diffusivities are given by K_T and K_S , and ν is the kinematic viscosity.

Since the density expressed in (2.2) and (2.9) depends on both temperature and salinity, we can write

$$\rho = \rho_{00} \left[1 + \frac{\rho_0}{\rho_{00}} + \frac{\rho'}{\rho_{00}} \right] , \quad (2.13)$$

as

$$\rho = \rho_{00} (1 - \alpha T_0 + \beta S_0 - \alpha T' + \beta S') , \quad (2.14)$$

where the coefficients of expansion are given by $\alpha = 1/T_{00}$ and $\beta = 1/S_{00}$ (Turner, 1973). Combining (2.2) and (2.14) and equating the background and convective parts, we get

$$\rho_0 = \rho_{00} (-\alpha T_0 + \beta S_0) = \rho_{00} (\alpha \Delta T - \beta \Delta S) z/z_T , \quad (2.15)$$

and

$$\rho' = \rho_{00} (-\alpha T' + \beta S') , \quad (2.16)$$

where the linear relation for ρ_0 is found by substituting (2.7) and (2.8) for S_0 and T_0 .

By introducing the stream function ψ , where $u' = -\partial\psi/\partial z$ and $w' = \partial\psi/\partial x$, and cross-differentiating (2.9) to eliminate pressure, we obtain the vorticity equation

$$\frac{\partial}{\partial t}(\nabla^2\psi) + J(\psi, \nabla^2\psi) = g\left[\alpha \frac{\partial T'}{\partial x} - \beta \frac{\partial S'}{\partial x}\right] + \nu \nabla^4\psi. \quad (2.17)$$

The thermodynamic equations for heat and salt can be rewritten as

$$\frac{\partial T'}{\partial t} + J(\psi, T') - \frac{\Delta T}{z_T} \frac{\partial \psi}{\partial x} = K_T \nabla^2 T', \quad (2.18)$$

$$\frac{\partial S'}{\partial t} + J(\psi, S') - \frac{\Delta S}{z_T} \frac{\partial \psi}{\partial x} = K_S \nabla^2 S', \quad (2.19)$$

where the Jacobian is defined as $J(f, g) = \frac{\partial f}{\partial x} \frac{\partial g}{\partial z} - \frac{\partial f}{\partial z} \frac{\partial g}{\partial x}$. With this notation, we can write the boundary conditions as

$$\psi = \frac{\partial^2 \psi}{\partial z^2} = T' = S' = 0 \text{ at } z = 0, z_T. \quad (2.20)$$

These constraints imply stress-free boundaries that are perfect conductors of heat and salt. In the horizontal, cyclic boundary conditions are assumed at $x = 0, L$.

2.2 Dimensionless Forms

We assume that the horizontal domain is infinite, and that the characteristic length in the x -direction is L . To simplify the Boussinesq system, we introduce the following dimensionless forms:

$$\psi = \psi^* K_T, \quad (2.21)$$

$$x = x^* L/2\pi, \quad (2.22)$$

$$z = z^* z_T/\pi, \quad (2.23)$$

$$t = t^* z_T L/2\pi^2 K_T, \quad (2.24)$$

$$T' = T^* \nu K_T T_{00} \pi^3/g z_T^3, \quad (2.25)$$

$$S' = S^* \nu K_T S_{00} \pi^3/g z_T^3, \quad (2.26)$$

where the starred variables are dimensionless. An aspect ratio a may be defined as

$$a = 2 z_T/L, \quad (2.27)$$

a Prandtl number as

$$P = \nu/K_T, \quad (2.28)$$

and a ratio τ of the diffusivities as

$$\tau = K_S/K_T. \quad (2.29)$$

To represent the forcing applied to the system, we define a salinity Rayleigh number

$$Ra_S = \frac{g \Delta S z_T^3}{\nu K_T S_{00} \pi^4} , \quad (2.30)$$

and a thermal Rayleigh number

$$Ra_T = \frac{g \Delta T z_T^3}{\nu K_T T_{00} \pi^4} . \quad (2.31)$$

Positive values of Ra_T and Ra_S represent a destabilizing temperature gradient and a stabilizing salinity gradient, respectively, as found in the diffusive regime. Here, both Ra_S and Ra_T are defined using K_T . This will present no difficulties in interpreting the results, and will also make the $\rho_0 = \text{constant}$ line correspond to the $Ra_T = Ra_S$ line (Section 2.3). The dimensionless Laplacian operator is given by

$$\tilde{\nabla}^2(\psi) = a^2 \frac{\partial^2(\psi)}{\partial x^{*2}} + \frac{\partial^2(\psi)}{\partial z^{*2}} . \quad (2.32)$$

Writing (2.17)-(2.19) in dimensionless form gives

$$\frac{\partial}{\partial t^*}(\tilde{\nabla}^2 \psi^*) + J(\psi^*, \tilde{\nabla}^2 \psi^*) = P \left[\frac{\partial T^*}{\partial x^*} - \frac{\partial S^*}{\partial x^*} \right] + \frac{P}{a} \tilde{\nabla}^2 \psi^* , \quad (2.33)$$

$$\frac{\partial T^*}{\partial t^*} + J(\psi^*, T^*) - Ra_T \frac{\partial \psi^*}{\partial x^*} = \frac{\tilde{\nabla}^2 T^*}{a} , \quad (2.34)$$

$$\frac{\partial S^*}{\partial t^*} + J(\psi^*, S^*) - Ra_S \frac{\partial \psi^*}{\partial x^*} = \frac{\tau}{a} \tilde{\nabla}^2 S^* . \quad (2.35)$$

The above introduction of dimensionless variables enables us to specify completely the system by knowing the values of the five dimensionless parameters P , a , Ra_T , Ra_S , and τ . For the diffusive regime, we study the case in which the values of both Rayleigh numbers are positive. Here, P and τ characterize the properties of the fluid, while Ra_T and Ra_S represent externally applied forcing rates (Huppert and Moore, 1976). From the properties of salt water, we find that $P = 7$ and $\tau = 0.01$. Thus the problem is reduced to one in the three parameters Ra_S , Ra_T , and a .

2.3 Linear Stability Analysis

Expressions characterizing some of the properties of the diffusive regime can be found using a linear stability analysis of the conductive state. Because this state is motionless, the Jacobian terms from (2.33)-(2.35) are dropped, producing the linear equations

$$\frac{\partial}{\partial t^*} (\tilde{v}^* \tilde{v}^*) = P \left[\frac{\partial T^*}{\partial x^*} - \frac{\partial S^*}{\partial x^*} \right] + \frac{P}{a} \tilde{v}^* \tilde{v}^* , \quad (2.36)$$

$$\frac{\partial T^*}{\partial t^*} - Ra_T \frac{\partial v^*}{\partial x^*} = \frac{\tilde{v}^* T^*}{a} , \quad (2.37)$$

$$\frac{\partial S^*}{\partial t^*} - Ra_S \frac{\partial v^*}{\partial x^*} = \frac{\tau}{a} \tilde{v}^* S^* . \quad (2.38)$$

We assume solutions of the form

$$v^* \sim e^{\lambda t} \sin(kx) \sin(nz) , \quad (2.39)$$

$$T^* \sim e^{\lambda t} \cos(kx) \sin(nz) , \quad (2.40)$$

$$S^* \sim e^{\lambda t} \cos(kx) \sin(nz) , \quad (2.41)$$

where k is a horizontal, integral wavenumber, and n is a vertical, integral wavenumber. Also, the eigenvalue λ is a complex number whose real part represents the growth rate and imaginary part represents the oscillatory behavior. Substituting (2.39)-(2.41) into (2.36)-(2.38) leads to the following characteristic equation:

$$\lambda^3 + \frac{\lambda^2 \epsilon}{a} (1 + P + \tau) - \frac{\lambda}{\epsilon} \left[P k^2 (Ra_T - Ra_S) - \frac{\epsilon^3}{a^2} (P + \tau P + \tau) \right] + \frac{P k^2}{a} (-Ra_T \tau + Ra_S) + \frac{\tau \epsilon^3 P}{a^3} = 0 , \quad (2.42)$$

where $\epsilon = a^2 k^2 + n^2$. When λ satisfies this cubic equation, a solution to (2.36)-(2.38) of the form (2.39)-(2.41) exists. Of the three roots to (2.42), one will always be real. The other two roots may be either real or complex conjugates (Baines and Gill, 1969).

To find the bifurcation point for the steady solution, where stability is lost by a negative eigenvalue becoming positive, and therefore going through zero, we substitute $\lambda = 0$ into (2.42) to give

$$Ra_{TC} = \frac{Ra_S}{\tau} + \frac{\epsilon^3}{a^2 k^2} . \quad (2.43)$$

Here, Ra_{Tc} represents the onset of an infinite number of steady solutions, one for each combination of horizontal and vertical wavenumbers. Exchanges of stability usually occur at such critical values of the forcing parameter, and these critical values are determined by other parameters of the system. We can minimize the value of Ra_{Tc} to find which parameter values give the smallest forcing rate required to balance energy input and dissipation (Laufersweiler, 1987).

The existence of a minimum value for Ra_{Tc} indicates that a preferred response is possible in the fluid. At a value of Ra_T less than its minimum critical value, perturbations of all wavelengths will damp because every eigenvalue is negative. At a value of Ra_T greater than the minimum critical value, some perturbations are able to grow. The perturbations that first grow give the preferred mode and are associated with a certain aspect ratio.

To minimize the magnitude of Ra_{Tc} , we differentiate (2.43) with respect to a^2k^2 to get

$$Ra_{Tmin} = \frac{Ra_S}{\tau} + \frac{27}{4} . \quad (2.44)$$

Here, Ra_{Tmin} is the minimum value of Ra_{Tc} for the development of steady convective flow and occurs when $a^2k^2 = 1/2$ and $n = 1$.

Physically, this corresponds to the minimum vertical temperature gradient required to support convection. We note that setting $Ra_S = 0$ in (2.43) and (2.44) gives the same expression for Ra_{Tc} and Ra_{Tmin} as those in Rayleigh-Bénard convection.

Since $\tau \ll 1$, the first term in (2.43) dominates when $Ra_S > 0.0675$, or for almost all values of Ra_S . This observation implies that the destabilizing temperature gradient must exceed the stabilizing salinity gradient by a factor of 100 before steady convection can occur (Veronis, 1965). However, satisfying this requirement would lead to a vertical density profile that is very unstable gravitationally. A bifurcation from a trivial solution directly to a steady one would require too large a difference between the temperature and salinity gradients. Intuitively, this result seems unphysical, leading us to ask whether other bifurcations are possible.

To find the transition from the conductive solution to a convective solution via a Hopf bifurcation, we let $\lambda = i\lambda_m$, where λ_m is real. Substituting this into (2.42) gives a complex cubic polynomial having real part

$$-\lambda_m^2 \frac{\epsilon^2}{a} (1 + P + \tau) + \frac{P \epsilon k^2}{a} (Ra_S - \tau Ra_T) + \frac{\tau \epsilon^4 P}{a^3} = 0, \quad (2.45)$$

and imaginary part

$$-\lambda_m^3 \xi - \lambda_m \left[P k^2 (Ra_T - Ra_S) - \frac{\xi^3}{a^2} (P + \tau P + \tau) \right] = 0 \quad . \quad (2.46)$$

To obtain the Hopf bifurcation points, we solve (2.46) for λ_m^2 and note that $\lambda_m^2 > 0$ must hold to guarantee the existence of the Hopf point. Putting (2.46) into (2.45) gives the following expression for H_k , the value of Ra_T at the Hopf bifurcation point:

$$H_k = \frac{Ra_S (P + \tau)}{1 + P} + \frac{(a^2 k^2 + n^2)^3 \left[(1 + \tau + \tau/P)(1 + \tau + P) - \tau \right]}{a^2 k^2 (1 + P)} \quad . \quad (2.47)$$

Here, (2.47) represents the onset of an infinite number of periodic solutions, one for each combination of horizontal and vertical wavenumbers. Since $\tau = 0.01$, and $P = 7$, (2.47) can be well approximated by

$$H_k \approx \frac{Ra_S P}{1 + P} + \frac{(a^2 k^2 + n^2)^3}{a^2 k^2} \quad . \quad (2.48)$$

To find the Hopf bifurcation point H_m at which the conductive regime undergoes a transition to a periodic regime of horizontal wavenumber m and vertical wavenumber 1, we set $k = m$ and $n = 1$ in (2.47). For the Hopf point H_j denoting the onset of a periodic solution of horizontal wavenumber j and vertical wavenumber 1, we set $k = j$, and $n = 1$. Figure 1 shows how the values of H_m and H_j vary

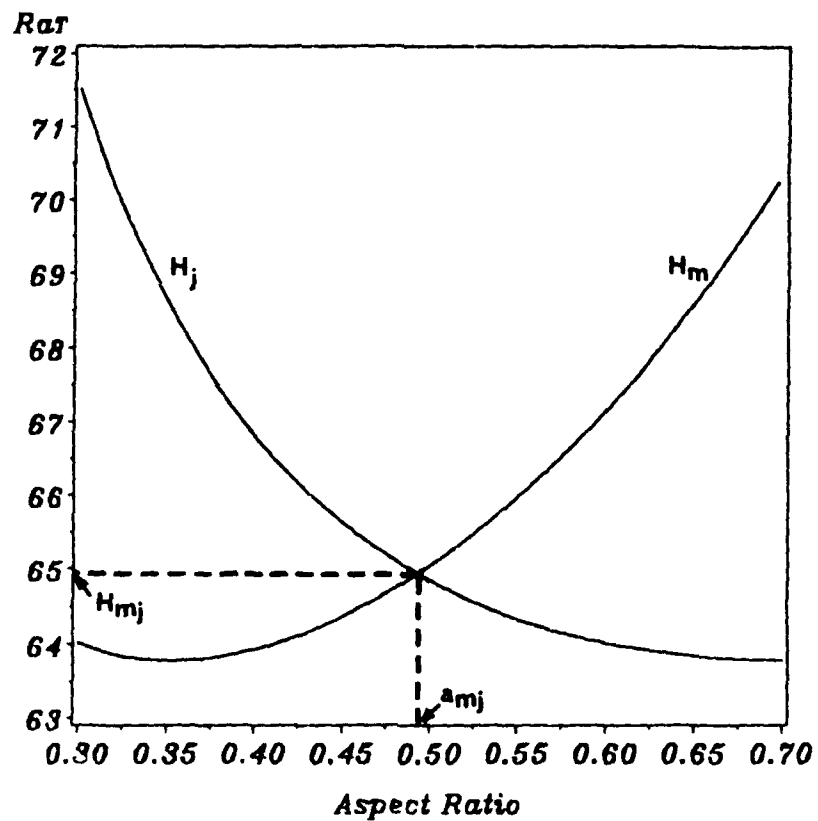


Figure 1 The dependence of the Hopf bifurcation points H_m and H_j on the aspect ratio where $Ra_S=65$, $m=2$, $j=1$, $P=7$, and $\tau=0.01$. These two curves intersect at the double Hopf point H_{mj} given approximately by $a_{mj}=0.49343$.

with a for the case of $m = 2$ and $j = 1$. In a system having two horizontal wavenumbers m and j , the double Hopf point H_{mj} occurs when the Hopf points H_m and H_j coincide and m -periodic and j -periodic solutions are created simultaneously. The aspect ratio a_{mj} at which the double Hopf point occurs is given by setting $k = m$ and $k = j$ in (2.47) and then equating the resulting right sides to give

$$a_{mj}^2 = \frac{m^{2/3} - j^{2/3}}{m^2 j^{2/3} - j^2 m^{2/3}} . \quad (2.49)$$

We note that this expression for a_{mj} matches that for double steady bifurcation in Rayleigh-Benard convection (Hirschberg, 1987). For $m = 2$ and $j = 1$, we find that $a_{mj} \approx 0.49343$. This point is of special interest since, if a toral solution is present, then it appears when the double Hopf point is separated into two single Hopf points by increasing or decreasing from a_{mj} the value of the aspect ratio a (Figure 1). We note that the five-coefficient Veronis (1965) model V_m or V_j of wavenumber m or j is not capable of supporting a double Hopf bifurcation, or a toral solution, since a toral solution requires two horizontal wavenumbers, and V_m or V_j contain only one.

In the absence of diffusion and viscosity, there is no Hopf bifurcation, and the vertical density distribution alone determines

the response of the fluid to small displacements (Figure 2). Above the line $Ra_S = Ra_T$ denoting the isopycnal case, a parcel displaced upwards will be lighter than its surroundings and its motion will exhibit exponential growth away from its initial position. Below this line, where density decreases with height, parcels will oscillate at the Brunt-Vaisala frequency. On the constant density line, a displaced parcel will have the same density as its surroundings and so will remain in its new position.

Adding diffusion and viscosity produces Hopf bifurcation points (2.47) (Figure 3). This Hopf bifurcation line is an adjustment to the constant density line. Now there is growth to a periodic solution above the Hopf line, and damped oscillations below this line. Adding dissipative forces allows damped oscillations when density increases with height at parameter values where exponential growth occurred in the inviscid case. In contrast, there are still periodic solutions at parameter values where, in the inviscid case, there were oscillations at the Brunt-Vaisala frequency.

The Hopf and steady bifurcation boundaries, as well as the $\rho_0 =$ constant line given by $Ra_T = Ra_S$, are shown in Figure 4. In regions A and B (shaded) of this figure, there is no development of motion, and all perturbations damp to the stable conductive solution. In region

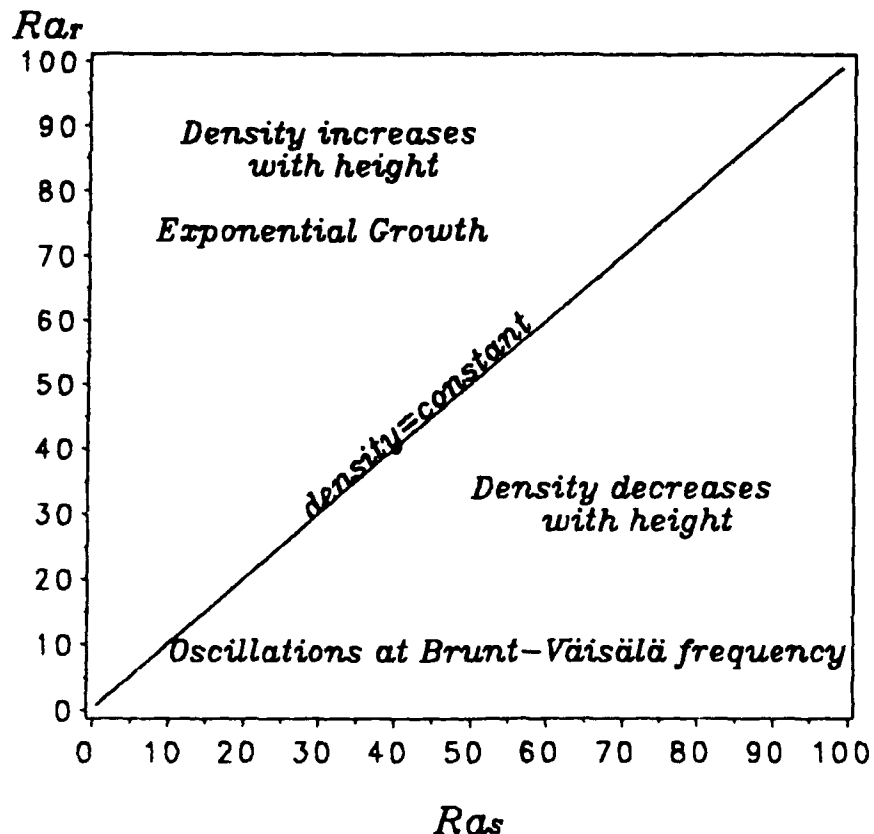


Figure 2 Convective regimes in the inviscid case where positive values of Ra_T and Ra_S represent destabilizing and stabilizing gradients, respectively. Displaced parcels in the regime above the isopycnal line $Ra_S = Ra_T$ will grow exponentially away from their initial positions, while those in the regime below the $Ra_S = Ra_T$ line will oscillate at the Brunt-Väisälä frequency.

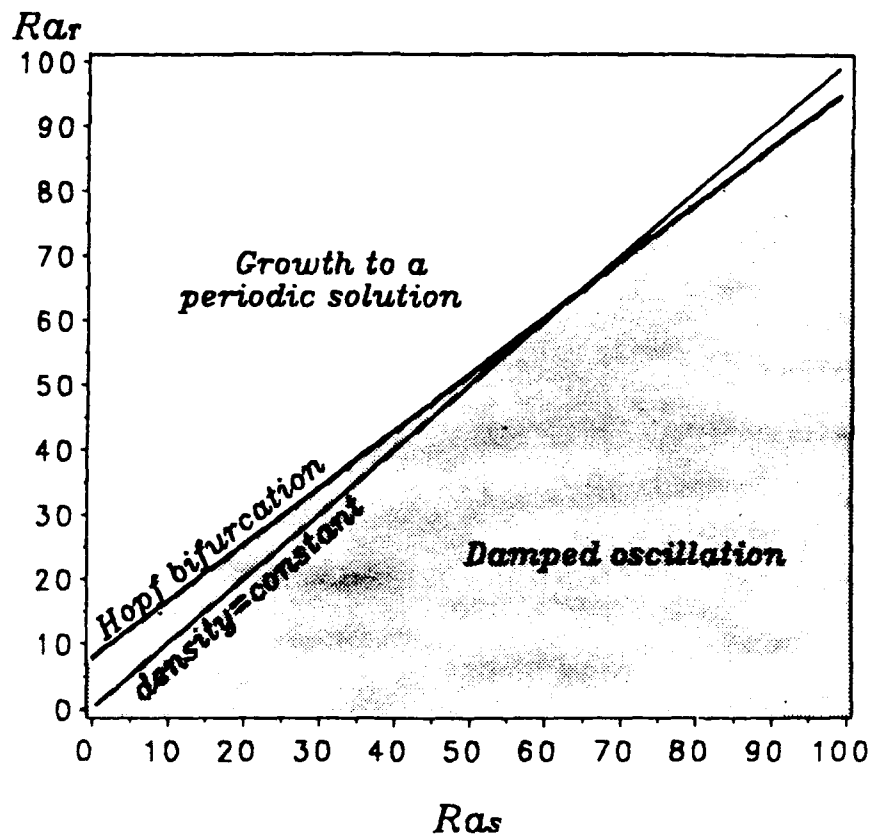


Figure 3 Convective (unshaded) and conductive (shaded) regimes when there are diffusion and viscosity. Adding these dissipative forces creates Hopf bifurcation points, which now separate the regimes. In the inviscid case (Figure 2), the constant density line divides the two regimes. The shaded area represents damped oscillations toward the conductive solution. Note that in some cases, adding these forces allows damped oscillations to occur even when density increases with height.

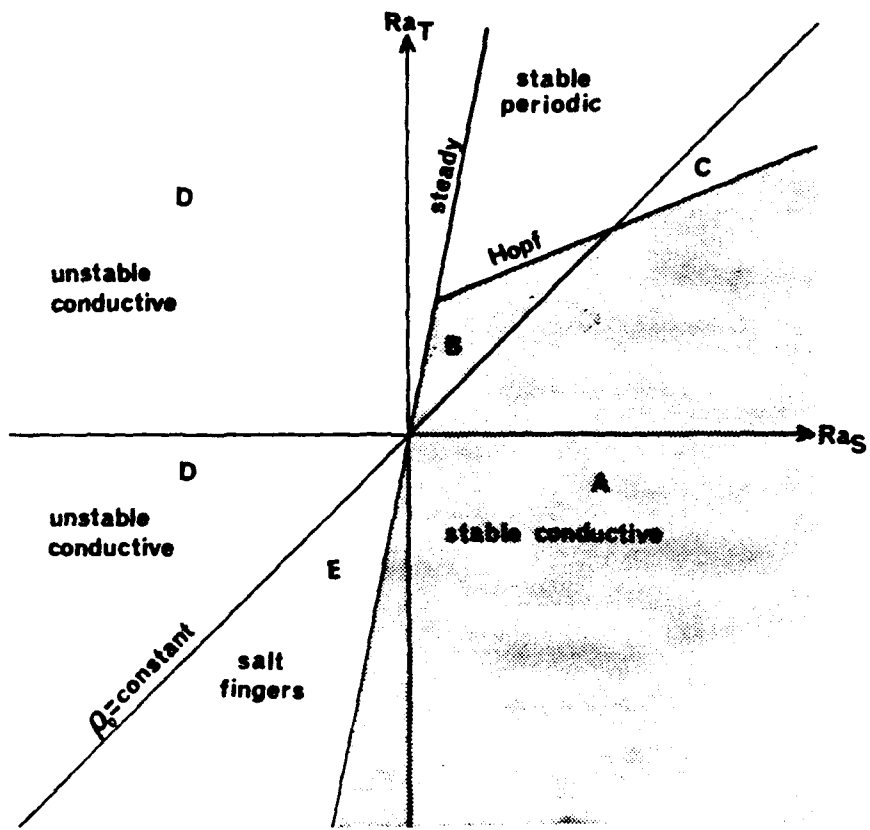


Figure 4 Schematic depiction of the convective (periodic), salt finger, and conductive regimes. The shaded area represents the stable conductive solution. The Hopf and steady lines denote periodic and steady bifurcation points, respectively, on the conductive solution. Regions A, B, C, D and E are discussed in the text (after Turner, 1973).

C, periodic solutions exist even though the density stratification is statically stable. All values in the regions labeled D correspond to growth from an unstable conductive state. In the upper right quadrant, or in the diffusive regime, values below the Hopf line correspond to stable conductive solutions (shaded), and points above the Hopf line correspond to stable periodic ones, as denoted in Figure 3. In region E, where both temperature and salinity increase with height, salt fingers are observed (Turner, 1973).

Region B in Figure 4 represents a fluid that is gravitationally unstable, since $Ra_T > Ra_S$, but one in which damped motion nevertheless does occur. This region corresponds to a gravitationally unstable case since in a nondiffusive fluid all displaced parcels will continue to depart from their initial position (Figure 2); yet in this region of Ra_T - Ra_S space the conductive state is stable. To understand how this situation comes about, we consider a parcel that is perturbed upwards in a diffusive fluid. In this case, it is saltier and warmer than its environment, as shown by position 1 in Figure 5. The greater, more rapidly diffusing parcel temperature equilibrates quickly with that of the surroundings of the parcel (position 2). Owing to the salinity difference still present, the parcel is heavier than its environment and so accelerates downward toward position 3B. The parcel will always overshoot its initial

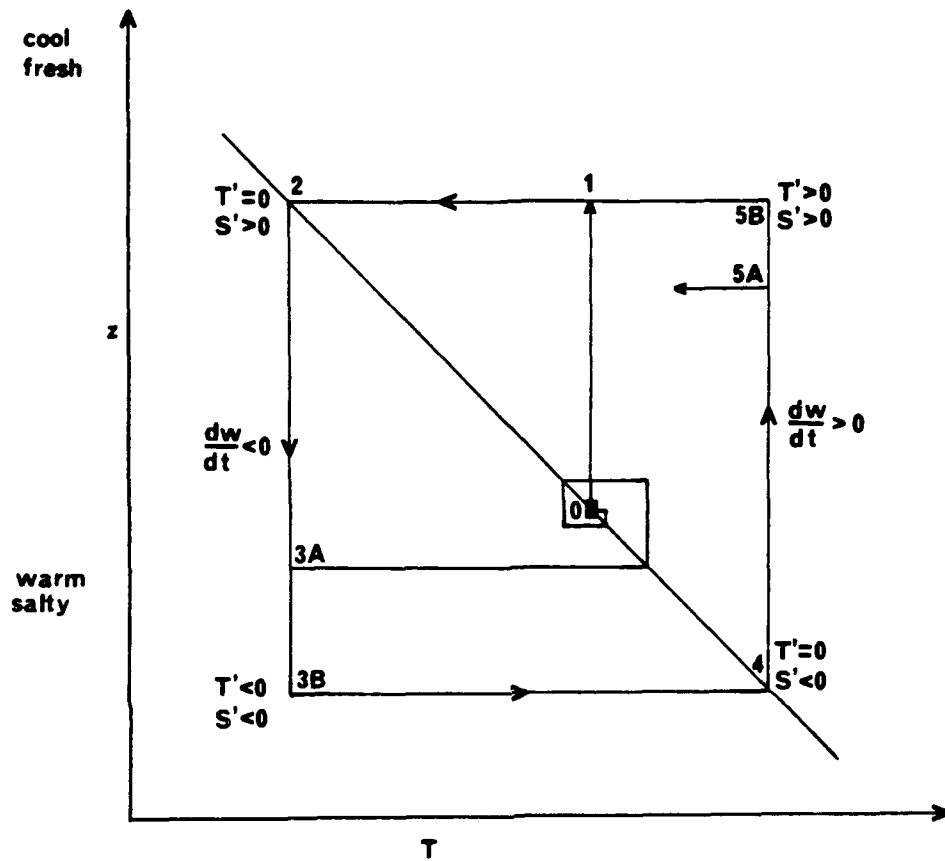


Figure 5 Schematic depiction of the motion of parcels in the stable conductive and periodic regimes. A parcel is perturbed upwards from position 0 to position 1. Comparing the parcel temperature and salinity to those of its environment will determine if the parcel returns to its original position via a damped oscillation (1,2,3A) or (1,2,3B,4,5A), or maintains a periodic solution (1,2,3B,4,5B).

position since by Archimedes Principle $dw/dt = g(\rho_e - \rho_p)/\rho_p$, where ρ_p is the density of the parcel and ρ_e is the density of the environment. This acceleration is evident in (2.9); since $dw/dt \sim \alpha T' - \beta S'$, either a negative temperature perturbation or a positive salinity perturbation will result in downward acceleration. In region B, the salinity gradient is not large enough to cause the parcel to attain position 3B in Figure 5; it reaches only position 3A. This causes a damped oscillation to the original position 0.

In region C, the fluid is stable, and $Ra_S > Ra_T$. Again, a parcel displaced upwards is warmer and saltier than its environment as shown by position 1 in Figure 5. As before, the temperature begins diffusing rapidly to that of the background state, equilibrating with its surroundings more rapidly than does the salt field and the parcel now moves to position 2. Again, it is heavier than its environment and sinks. It travels below its original position to location 3B, and is now fresher and colder than its surroundings. With the salinity gradient sufficiently large, the above process continues, and a stable oscillation is seen. Here, a density distribution decreasing upwards does not imply a decaying solution.

2.4 The Spectral Model

To develop the nonlinear, low-order spectral model, we need functions for ψ^* , T^* , and S^* that can describe the convective motion with a small number of terms that satisfy the boundary conditions (2.20). Because of the cyclic, stress-free boundary conditions, and rectangular domain, trigonometric functions suffice. With wavenumbers $n = 1$ and $n = 2$ in the vertical and wavenumbers m, j , $m-j$, and $m+j$ in the horizontal, the stream function can be represented in the following equation:

$$\begin{aligned}\psi^*(x^*, z^*, t^*) = & \psi_{m1}(t^*) \sin(mx^*) \sin(z^*) + \psi_{j1}(t^*) \sin(jx^*) \sin(z^*) + \\ & \psi_{m-j,2}(t^*) \sin[(m-j)x^*] \sin(2z^*) + \\ & \psi_{m+j,2}(t^*) \sin[(m+j)x^*] \sin(2z^*) .\end{aligned}\quad (2.50)$$

The time-dependent coefficients are amplitudes, and these are found numerically by integrating the ordinary differential system composing the model. The four harmonics are chosen to allow the possibility for an exchange of stability between a primary periodic solution P_m of wavenumber m and a primary periodic solution P_j of wavenumber j ; this exchange occurs via the catalytic $(m-j, 2)$, $(m+j, 2)$ terms at the diffeo-Hopf points D_m and D_j (Chang and Shirer, 1984; Wells and Shirer, 1987). Stability is transferred from a solution dominated by

one horizontal wavenumber to one dominated by another wavenumber and can be represented by a secondary branch S_{mj} emanating from a primary one (Figure 6). As occurs in rotating convection, we expect that a two-torus appears via a secondary branch bifurcating from one of the primary periodic solutions (Wells and Shirer, 1987).

From the temperature term in the vertical velocity equation (2.9) and the vertical velocity term in the thermodynamic equation (2.11), we see that w' , or $\partial\psi/\partial x$, and T need the same phasing to include a heat flux term crucial to convection. Thus, we may write the temperature field as

$$T^*(x^*, z^*, t^*) = T_{m1}(t^*)\cos(mx^*)\sin(z^*) + T_{j1}(t^*)\cos(jx^*)\sin(z^*) + \\ T_{m-j,2}(t^*)\cos[(m-j)x^*]\sin(2z^*) + \\ T_{m+j,2}(t^*)\cos[(m+j)x^*]\sin(2z^*) + \\ T_{02}(t^*)\sin(2z^*) + T_{04}(t^*)\sin(4z^*) , \quad (2.51)$$

and the salinity field as

$$S^*(x^*, z^*, t^*) = S_{m1}(t^*)\cos(mx^*)\sin(z^*) + S_{j1}(t^*)\cos(jx^*)\sin(z^*) + \\ S_{m-j,2}(t^*)\cos[(m-j)x^*]\sin(2z^*) + \\ S_{m+j,2}(t^*)\cos[(m+j)x^*]\sin(2z^*) + \\ S_{02}(t^*)\sin(2z^*) + S_{04}(t^*)\sin(4z^*) . \quad (2.52)$$

Further, these cosine terms match those from the $\partial\psi^*/\partial x^*$ terms in the thermodynamic and vorticity equations. With representations this

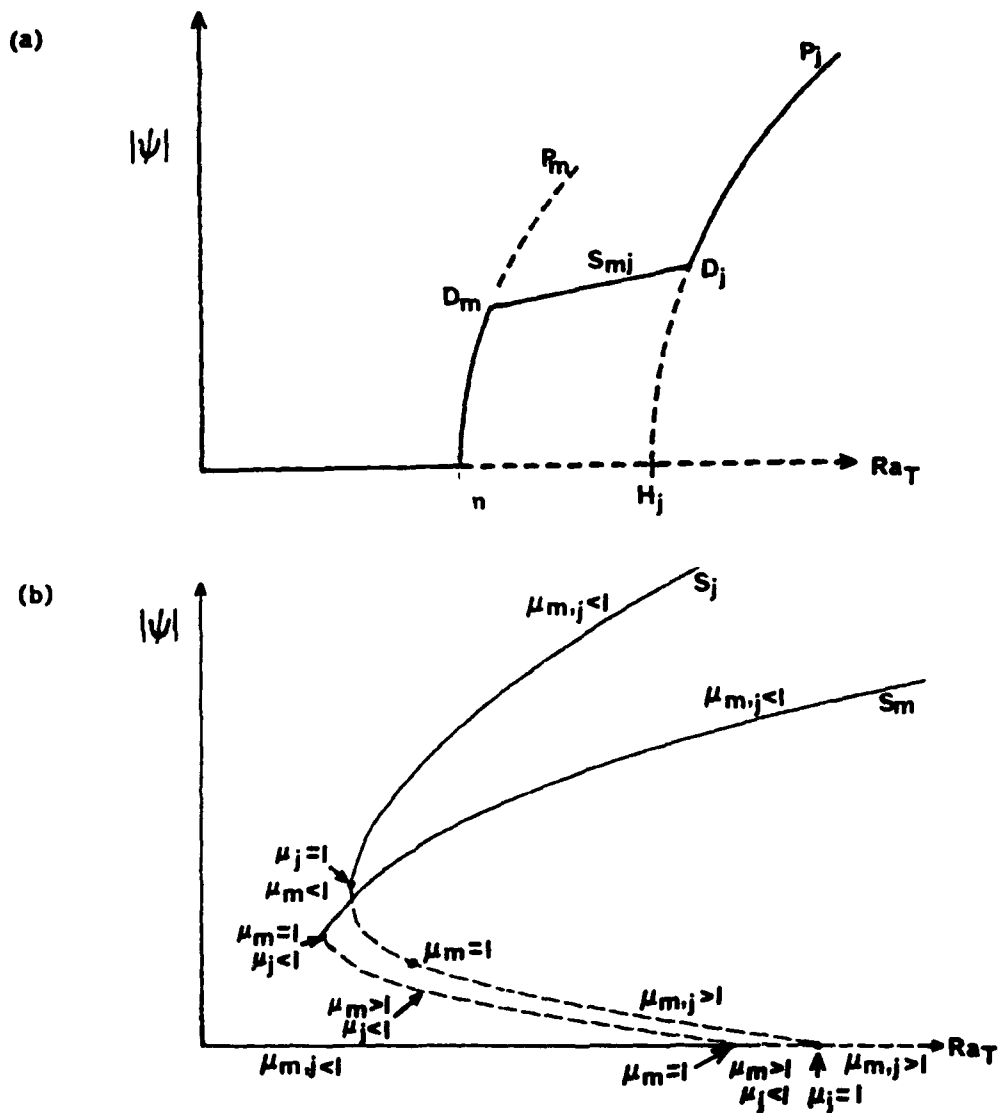


Figure 6 Schematic bifurcation diagrams showing (a) periodic and toral and (b) steady solutions of horizontal wavenumbers m and j . The solid curves represent stable solutions, and the dashed curves denote unstable ones. The periodic branches P_m and P_j are characterized by Hopf (H_k) and diffeo-Hopf (D_k) points where $k=m$ or j , and a secondary toral solution S_{mj} . The magnitudes of the characteristic multipliers μ_m and μ_j corresponding to the steady bifurcation points on the conductive solution and the steady regular turning points on the steady solutions S_m and S_j are shown in (b).

general, $\iint w^* T^* dx^* dz^* \neq 0$ is possible. Recall that background profiles are horizontal averages of the variables. Thus, it is the T_{02} , T_{04} , S_{02} , and S_{04} terms that represent the nonlinear distortions by the rolls of the linear background temperature T_0 and salinity S_0 fields. Also, the $(m,1)$, $(j,1)$, $(m+j,2)$, and $(m-j,2)$ wavenumber pairs included in the expansions (2.50)-(2.52) are only four of the infinite number of wavenumber pairs represented by the partial differential equations.

Upon substituting these Fourier series for ψ^* , T^* , and S^* into the dimensionless equations of motion (2.36)-(2.38), we can create the spectral model using the Galerkin technique (Higgins, 1987). The number of ordinary differential equations in this model is determined by the total number of coefficients in the expansions--sixteen in this case:

$$\dot{S}_{m1} = m\psi_{m1}S_{02} - \frac{1}{4}(m-j)\psi_{j1}S_{m+j,2} - \frac{1}{4}(m+j)\psi_{m-j,2}S_{j1} + \frac{1}{4}(m+j)\psi_{j1}S_{m-j,2} - \frac{1}{4}(m-j)\psi_{m+j,2}S_{j1} + Ra_S\psi_{m1}m - \frac{\tau}{a}S_{m1}(m^2a^2+1) , \quad (2.53)$$

$$\dot{S}_{j1} = j\psi_{j1}S_{02} + \frac{1}{4}(m+j)\psi_{m1}S_{m-j,2} + \frac{1}{4}(m-j)S_{m+j,2}\psi_{m1} + \frac{1}{4}(m+j)S_{m1}\psi_{m-j,2} + \frac{1}{4}(m-j)\psi_{m+j,2}S_{m1} + Ra_S\psi_{j1}j - \frac{\tau}{a}S_{j1}(j^2a^2+1) , \quad (2.54)$$

$$\begin{aligned}\dot{S}_{m-j,2} = & -\frac{1}{4}(m+j)\psi_{m1}S_{j1} - \frac{1}{4}(m+j)\psi_{j1}S_{m1} + 2(m-j)\psi_{m-j,2}S_{04} + \\ & Ra_S(m-j)\psi_{m-j,2} - \frac{\tau}{a}S_{m-j,2}[(ma-ja)^2 + 4] ,\end{aligned}\quad (2.55)$$

$$\begin{aligned}\dot{S}_{m+j,2} = & -\frac{1}{4}(m-j)\psi_{m1}S_{j1} + \frac{1}{4}(m-j)\psi_{j1}S_{m1} + 2(m+j)\psi_{m+j,2}S_{04} + \\ & Ra_S(m+j)\psi_{m+j,2} - \frac{\tau}{a}S_{m+j,2}[(ma+ja)^2 + 4] ,\end{aligned}\quad (2.56)$$

$$\dot{S}_{02} = -\frac{1}{2}m\psi_{m1}S_{m1} - \frac{1}{2}j\psi_{j1}S_{j1} - \frac{4\tau}{a}S_{02} ,\quad (2.57)$$

$$\dot{S}_{04} = -(m-j)\psi_{m-j,2}S_{m-j,2} - (m+j)\psi_{m+j,2}S_{m+j,2} - 16\frac{\tau}{a}S_{04} ,\quad (2.58)$$

$$\begin{aligned}\dot{T}_{m1} = & m\psi_{m1}T_{02} - \frac{1}{4}(m-j)\psi_{j1}T_{m+j,2} - \frac{1}{4}(m+j)\psi_{m-j,2}T_{j1} + \frac{1}{4}(m+j)\psi_{j1}T_{m-j,2} - \\ & \frac{1}{4}(m-j)\psi_{m+j,2}T_{j1} + Ra_T\psi_{m1} - \frac{1}{a}T_{m1}(m^2a^2+1) ,\end{aligned}\quad (2.59)$$

$$\begin{aligned}\dot{T}_{j1} = & j\psi_{j1}T_{02} + \frac{1}{4}(m+j)\psi_{m1}T_{m-j,2} + \frac{1}{4}(m-j)\psi_{m+j,2}T_{m1} + \frac{1}{4}(m+j)\psi_{m1}T_{m-j,2} + \\ & \frac{1}{4}(m-j)\psi_{m+j,2}T_{m1} + Ra_T\psi_{j1} - \frac{1}{a}T_{j1}(j^2a^2+1) ,\end{aligned}\quad (2.60)$$

$$\begin{aligned}\dot{T}_{m-j,2} = & -\frac{1}{4}(m+j)\psi_{m1}T_{j1} - \frac{1}{4}(m+j)\psi_{j1}T_{m1} + 2(m-j)\psi_{m-j,2}T_{04} + \\ & (m-j)Ra_T\psi_{m-j,2} - \frac{1}{a}T_{m-j,2}[(ma-ja)^2 + 4] ,\end{aligned}\quad (2.61)$$

$$\begin{aligned}\dot{T}_{m+j,2} = & -\frac{1}{4}(m-j)\psi_{m1}T_{j1} + \frac{1}{4}(m-j)\psi_{j1}T_{m1} + 2(m+j)\psi_{m+j,2}T_{04} + \\ & (m+j)Ra_T\psi_{m+j,2} - \frac{1}{a}T_{m+j,2}[(ma+ja)^2 + 4] ,\end{aligned}\quad (2.62)$$

$$\dot{T}_{02} = -m \frac{1}{2} \psi_{m1} T_{m1} - \frac{1}{2} j \psi_{j1} T_{j1} - \frac{4}{a} T_{02} , \quad (2.63)$$

$$\dot{T}_{04} = -(m-j) \psi_{m-j,2} T_{m-j,2} - (m+j) \psi_{m+j,2} T_{m+j,2} - 16 \frac{1}{a} T_{04} , \quad (2.64)$$

$$\dot{\psi}_{m1} = \frac{\psi_{j1} \psi_{m-j,2} (m^3 a^2 - m^2 j a^2 - 2m j^2 a^2 + 3m + 3j)}{4(m^2 a^2 + 1)} + \frac{\psi_{j1} \psi_{m+j,2} (-m^3 a^2 - m^2 a^2 j + 2m j^2 a^2 - 3m + 3j)}{4(m^2 a^2 + 1)}$$

$$2m j^2 a^2 - 3m + 3j) + \frac{Pm}{(m^2 a^2 + 1)} (T_{m1} - S_{m1}) - \frac{P\psi_{m1}}{a} (m^2 a^2 + 1) , \quad (2.65)$$

$$\dot{\psi}_{j1} = \frac{\psi_{m1} \psi_{m-j,2} (-j^3 a^2 + m j^2 a^2 + 2j m^2 a^2 - 3m - 3j)}{4(j^2 a^2 + 1)} + \frac{\psi_{m1} \psi_{m+j,2} (-j^3 a^2 - j^2 a^2 m + 2j m^2 a^2 + 3m - 3j)}{4(j^2 a^2 + 1)} + \frac{P\psi_{j1}}{a} (j^2 a^2 + 1) , \quad (2.66)$$

$$\dot{\psi}_{m-j,2} = \frac{\psi_{m1} \psi_{j1} a^2 (-m^3 - m^2 j + m j^2 + j^3)}{4[a^2(m-j)^2 + 4]} + \frac{P(m-j)(T_{m-j,2} - S_{m-j,2})}{a^2(m-j)^2 + 4} - \frac{P}{a} \psi_{m-j,2} [a^2(m-j)^2 + 4] , \quad (2.67)$$

$$\dot{\psi}_{m+j,2} = \frac{\psi_{m1} \psi_{j1} a^2 (m^3 - m^2 j - m j^2 + j^3)}{4[a^2(m+j)^2 + 4]} + \frac{P(m+j)(T_{m+j,2} - S_{m+j,2})}{a^2(m+j)^2 + 4} - \frac{P}{a} \psi_{m+j,2} [a^2(m+j)^2 + 4] . \quad (2.68)$$

The modification of the background temperature and salinity fields arises from the interaction of modes via the nonlinear, or Jacobian terms, in the equations of motion. For example, the nonlinear product $T_{m1} \psi_{m1}$ modifies the T_{02} term in (2.63), since

adding the vertical wavenumbers and subtracting the horizontal wavenumbers gives the 02 mode. Likewise, for T_{04} , the product $T_{m+j,2}\psi_{m+j,2}$ modifies the T_{04} term in (2.64). A higher order spectral model would be necessary to produce changes in terms such as T_{01} and T_{03} . Thus, a nonlinear model is needed to represent the changes in the mean background temperature and salinity profiles.

The above differential system (2.53)-(2.68) contains two primary periodic solutions of the form in the Veronis (1965) five-coefficient model V_m ,

$$P_m = (S_{m1}, 0, 0, 0, S_{02}, 0, T_{m1}, 0, 0, 0, T_{02}, 0, \psi_{m1}, 0, 0, 0), \quad (2.69)$$

and that in V_j ,

$$P_j = (0, S_{j1}, 0, 0, S_{02}, 0, 0, T_{j1}, 0, 0, T_{02}, 0, 0, \psi_{j1}, 0, 0), \quad (2.70)$$

as well as two other periodic solutions

$$P_{m-j} = (0, 0, S_{m-j,2}, 0, 0, S_{04}, 0, 0, T_{m-j,2}, 0, 0, T_{04}, 0, 0, \psi_{m-j,2}, 0), \quad (2.71)$$

and

$$P_{m+j} = (0, 0, 0, S_{m+j,2}, 0, S_{04}, 0, 0, 0, T_{m+j,2}, 0, T_{04}, 0, 0, 0, \psi_{m+j,2}). \quad (2.72)$$

The five-coefficient steady solutions from the Veronis model are also included in this truncation.

In the Veronis model, the primary branches (2.69) and (2.70) bifurcate from the conductive solution at the Hopf points that were

calculated using (2.47) for the partial differential equations. The five-coefficient periodic solutions P_m and P_j will be essential for deciding whether toral or other solutions are possible. We will find these solutions using an eigenvalue analysis, with which we may also determine the stability of the periodic solutions P_m and P_j . With this stability analysis, we can show when either five-coefficient branch loses stability to perturbations of different wavenumbers, as represented by the other eleven coefficients. From this eigenvalue analysis, we can also diagnose what type of solution gains stability when the five-coefficient branch loses stability. Of particular interest would be the toral solution that gains stability at a diffeo-Hopf bifurcation. These properties are discussed in Chapter 3.

Chapter 3

FINDING BIFURCATION POINTS ON PERIODIC SOLUTIONS

To discover when a new solution bifurcates from a temporally periodic one, we need to determine the stability of the temporally periodic branch (Feldstein, 1987). It is sufficient to show that a new solution is created when this primary branch loses stability at a certain value of the forcing rate. Determination of both the stability of the periodic solution and the character of the new branching solution is performed via an eigenvalue analysis of an appropriate system of perturbation equations. By examining these eigenvalues, or characteristic multipliers μ_n , as the forcing rate is varied, we are able to find diffeo-Hopf points that signal bifurcation to a torus, as well as other bifurcation points, on the periodic solution. The behavior of the characteristic multipliers at the bifurcation points reveals the type of new solution emanating from the periodic one.

3.1 Stability of a Periodic Solution

To determine the stability of a periodic solution, we superimpose a perturbation on that solution and determine whether the perturbation grows or decays. If this perturbation grows, then the

periodic solution is unstable, and if it decays, then the solution is stable.

We can write the sixteen-coefficient model (2.53)-(2.68) in the form

$$\dot{y}_i = f_i(y_1, y_2, \dots, y_{16}, Ra_S, Ra_T, a, \tau, P, m, j), \quad i=1, \dots, 16, \quad (3.1)$$

which has a periodic solution $y_i(t) = P_i(t)$ of period T (Feldstein, 1987). We then consider perturbations $x_i(t)$ of $P_i(t)$ and write

$$y_i(t) = P_i(t) + x_i(t), \quad i=1, \dots, 16. \quad (3.2)$$

By knowing whether $|x_i(t)|$ increases or decreases, we can determine the stability of $P_i(t)$.

To obtain a set of equations that describes how these perturbations change with time, we substitute (3.2) into (3.1). For example, we let $S_{m1}^p(t) = S_{m1}^p + x_1$, $\psi_{m1}^p(t) = \psi_{m1}^p + x_{13}$, etc., where the superscript p denotes a periodic solution, and substitute these into (2.53). To linearize about $P_i(t)$, we assume that $|x_i(t)|$ remains small and so drop products of the perturbations. After equating the periodic and perturbation terms, we get

$$\begin{aligned} \dot{S}_{m1}^p(t) = & -\frac{1}{4}(m-j)\psi_{j1}^p S_{m+j,2}^p - \frac{1}{4}(m+j)\psi_{m-j,2}^p S_{j1}^p + \frac{1}{4}(m+j)S_{m-j,2}^p \psi_{j1}^p - \\ & \frac{1}{4}(m-j)\psi_{m+j,2}^p S_{j1}^p + m\psi_{m1}^p S_{02}^p + mRa_S\psi_{m1}^p - (\tau/a)S_{m1}^p(m^2a^2 + 1), \quad (3.3) \end{aligned}$$

and

$$\begin{aligned}
 \dot{x}_i(t) = & -\frac{1}{4}(m-j)[x_{14}^p S_{m+j,2} + x_4^p \psi_{j1}] - \frac{1}{4}(m+j)[x_{15}^p S_{j1} + x_2^p \psi_{m-j,2}] + \\
 & \frac{1}{4}(m+j)[x_{14}^p S_{m-j,2} + x_3^p \psi_{j1}] - \frac{1}{4}(m-j)[x_2^p \psi_{m+j,2} + x_{16}^p S_{j1}] + mRa_S x_{13} \\
 & + m(x_{13}^p S_{02} + x_5^p \psi_{m1}) - (\tau/a)x_1(m^2 a^2 + 1) . \tag{3.4}
 \end{aligned}$$

We note that (3.3) is the periodic version of (2.53), and that the last three terms of (3.3) are those of the Veronis model V_m . Also, (3.4) is linear in the perturbation variables x_i . The other fifteen pairs of equations are formed in a similar way.

The resulting thirty-two-coefficient system S consists of the original sixteen-coefficient model (2.53) - (2.68) and a set of sixteen perturbation equations. The system of perturbation equations admits of the trivial solution, while the first sixteen give the periodic solution. To find the behavior of the perturbation components x_i , we need not know the periodic solution analytically. In this case, the first sixteen equations give the periodic solution numerically, and these values feed into the sixteen perturbation equations for the stability calculation. By calculating the eigenvalues μ_n , $n=1, \dots, 16$, of a matrix derived from solutions to this system evaluated at one period, we can determine if the

perturbation of the periodic solution in the sixteen-coefficient model is growing or decaying in any of the sixteen dimensions (Feldstein, 1987). We outline how we calculate the values of these characteristic multipliers in the next section.

3.2 Eigenvalue Calculation and Analysis

Given a five-coefficient periodic solution P_m or P_j , we would like to know those parameter values for which this solution is stable within the sixteen-coefficient model, those for which it is unstable, and the type of solution that replaces the periodic one when it becomes unstable. From the eigenvalue analysis of the integrated perturbation system discussed in Section 3.1, all of this information can be determined.

The initial conditions for each integration of the thirty-two-equation system S are specified in the following way. The first sixteen coefficients of S are chosen to be on the primary branch P_m or P_j which is being studied. Because these branches are solutions to the full system, the appropriate five Veronis coefficients are nonzero, the other eleven coefficients are zero, and these eleven will not grow numerically. The equations composing the second half of S are set to the value one in the perturbation component x_k with

all others set at zero; the result is integrated for one period T . This procedure is repeated for each value of $k=1, \dots, 16$ to produce final values $[x_i(t)]_k$, $i=1, \dots, 16$, after one period. These values are written as the entries of a matrix B . For example, to find the first column $k=1$, the initial conditions for the perturbation equations are $(x_1, x_2, \dots, x_{16})^T = (1, 0, \dots, 0)^T$. These integrations are performed sixteen times, one for each set of initial conditions involving only one nonzero perturbation component. The resulting sixteen columns yield the matrix B of perturbations evaluated at one period T :

$$B = \begin{bmatrix} k=1 & 2 & \dots & 16 \\ b_{11} & b_{12} & \dots & b_{1,16} \\ b_{21} & b_{22} & \dots & b_{2,16} \\ \cdot & \cdot & & \cdot \\ \cdot & \cdot & & \cdot \\ \cdot & \cdot & & \cdot \\ b_{16,1} & b_{16,2} & \dots & b_{16,16} \end{bmatrix}. \quad (3.5)$$

The eigenvalues μ_n of matrix B give the desired stability information. Recall that if these eigenvalues all have magnitude less than one, then the periodic solution is stable (Feldstein, 1987). As we note below, this matrix can be separated into a 5×5 , a 9×9 , and two 1×1 matrices without changing the values of the characteristic multipliers. One eigenvalue of B will equal one,

indicating integration for one period. If the model is integrated for one timestep δt instead of one period, then the eigenvalues of matrix $B(\delta t)$ give instantaneous divergence rates (Nese, 1989).

After determining the Hopf points H_m and H_j analytically from (2.47), we can integrate the five-coefficient Veronis model V_m or V_j for values of Ra_T that are slightly greater than those for H_m or H_j to find a periodic branch P_m or P_j (cf. Figure 6). Because the five nonzero components of the Veronis model V_k , $k = m$ or j , also produce a solution to the sixteen-coefficient model (2.53)-(2.68) with the other eleven components set to zero, it is much easier and faster to integrate the five-coefficient model V_k than the original sixteen-coefficient model. Whenever we are able to find P_m or P_j numerically, then it follows that these solutions are stable relative to perturbations involving the five components of the Veronis model.

After integrating the sixteen-coefficient system, we may separate it into four subsystems linearized about P_m or P_j . That is, we may rewrite the linearized system as

$$x = \frac{d}{dt} \begin{bmatrix} \underline{c} \\ \underline{d} \\ \underline{S}'_{04} \\ \underline{T}'_{04} \end{bmatrix} = \begin{bmatrix} C & 0 & & \\ 0 & D & 0 & \\ 0 & -16\tau/a & 0 & \\ & 0 & -16/a & \end{bmatrix} \begin{bmatrix} \underline{c} \\ \underline{d} \\ \underline{S}'_{04} \\ \underline{T}'_{04} \end{bmatrix}. \quad (3.6)$$

Here, \underline{c} denotes perturbations of the components of V_k , \underline{d} denotes perturbations in the 9x9 system, and S'_{04} and T'_{04} represent perturbations of the S_{04} and T_{04} terms, respectively. From (3.6) it is easy to see that S'_{04} and T'_{04} decay to zero according to

$$S'_{04} = S'_{04}(0)e^{(-16\pi t/a)}, \quad (3.7)$$

and

$$T'_{04} = T'_{04}(0)e^{(-16t/a)}. \quad (3.8)$$

Spectrally, the periodic solutions will always be stable to perturbations in these directions; the corresponding eigenvalues will always have magnitude less than one. Now the stability analysis has been reduced to evaluating the properties of the matrices C and D. Here, C is a 5x5 time-dependent matrix containing the terms from V_m or V_j , and D is a 9x9 matrix. As a check, C and D can also be found by separate integrations, and the eigenvalues of these matrices should be the same as those found when integrating the entire system S. Since the single wavenumber models V_m or V_j cannot contain a toral solution, the stability information for secondary branching to a torus is found in matrix D.

Since the eigenvalues measure expansion or contraction relative

to the orbit P_m or P_j , one eigenvalue μ_1 , which measures variations in the direction of the orbit, should always equal one; this eigenvalue is found in the 5x5 submatrix. The existence of $\mu_1=1$ provides a very useful check on the accuracy of the calculations. If μ_1 is slightly greater than or less than one, then it may indicate that the timestep used in the integration is too large or the number of iterations is too small, causing the integration to stop just before or just after one period.

If the periodic solution is determined numerically, then the period can only be known approximately. Therefore, a careful analysis of the magnitude of the period, and the appropriate number N of intervals needed to divide it, is necessary to determine the optimal timestep Δt . Here, the number of required timesteps is usually between 13,000 and 20,000, with a timestep Δt on the order of 10^{-4} . This is sufficient to yield $\mu_1 = 1 \pm 0.01$ and to approximate $|\Delta \psi_{k1}| = [\psi_{k1}(t=0) - \psi_{k1}(t=T)]/\psi_{k1}(t=0)$ to order 10^{-4} . The sensitivity of the five largest eigenvalues is illustrated in Table 1.

Table 1 contains eigenvalues calculated using two different timesteps Δt and lengths of integration N . The best approximation is the one in the third column, since $|\Delta \psi_{k1}|$ is the smallest. Here, the

Table 1 Estimates of the five largest eigenvalues μ_i for $Ra_S = 5.0$, $Ra_T = 12.8$, $H_m = 12.25$, $a = 0.486$, $m = 2$, and $j = 1$ for different timesteps Δt and iterates N in the integration. The first three eigenvalues are from integrating the 5×5 subsystem involving matrix C in (3.6) for the Veronis P_m solution, and the next three are from the 9×9 subsystem involving the matrix D . Also, T_a is the approximate period where $T_a = N\Delta t$ (cf. Figure 8).

Δt	3×10^{-4}	3×10^{-4}	2.2×10^{-4}	2.2×10^{-4}
N	15366	15360	20953	20954
T_a	4.6098	4.6080	4.6096	4.6099
$ \Delta v_{k_1} $	2.40×10^{-3}	3.15×10^{-2}	2.15×10^{-4}	3.89×10^{-3}
μ_1	1.01960	0.99368 $-0.02537i$	1.0179	1.0205
μ_2	0.96993	0.99368 $+0.02537i$	0.97146	0.96911
μ_3	0.09332	0.09323	0.09331	0.09333
μ_4	2.01620	2.01100	2.01580	2.01640
$\mu_{5,6}$	-0.09066 $\pm 0.32414i$	-0.089793 $\pm 0.32473i$	-0.090600 $\pm 0.32419i$	-0.09070 $\pm 0.32411i$
.
.

eigenvalue that indicates one period of integration is μ_1 . After integrating one more timestep (column four), we see that $|\Delta\psi_{k_1}|$ has increased 15.5 times, indicating a loss of two decimal places of accuracy in the estimate of $\psi_{k_1}(T)$. Also, the most important eigenvalues, which are those close to one in magnitude, change in the second decimal place as the model is integrated an extra timestep. We note that ψ must be known to four decimal places to get the eigenvalues accurate to two decimal places.

As the timestep is increased to 3.0×10^{-4} (columns one and two), the behavior of the first two eigenvalues is deceiving. As the number of integrations decreases, the first two eigenvalues become complex and have a magnitude near one, which is indicative of a diffeo-Hopf bifurcation. Knowing that we must have one eigenvalue equal to one, however, we conclude that this cannot be a complex conjugate pair. Also, the imaginary part is quite small. With a better approximation to the period, we see that one of these eigenvalues is signaling the occurrence of either a harmonic bifurcation or a periodic regular turning point, since we are far from the Hopf bifurcation point, and the other indicates that we have integrated for one period. This conclusion would change if we were close to H_k , because in this case there is also an eigenvalue having

magnitude near one and decreasing as we move away from H_k . The errors in the values of μ_i that are illustrated in Table 1 become greatly magnified for large values of $|\Delta\psi_{k_1}|$, i.e. before an accurate value of the period has been determined.

The other fifteen eigenvalues determine the stability of the primary branch, and depend sensitively on how accurately the value of the period is known. These characteristic multipliers also indicate which type of new solution has bifurcated from the primary branch. Three types of new solutions are possible, as we review below.

3.2.1 Subharmonic Bifurcation

If a real eigenvalue $\mu_\ell = -1$ occurs, then a subharmonic, or period doubling, bifurcation is signaled (Ruelle, 1989). The eigenvalue $\mu_\ell = -1$ implies that an eigenvector of the linearized system has been rotated 180° after one period T . Thus, the orbit has twice as far to go to complete one cycle. Because it requires twice the time to return to its original position, the bifurcation is called a period doubling bifurcation and the period of the new solution is approximately $2T$. In this case, there is only one new periodic solution that gains stability from the old one (Sparrow, 1982; Feldstein, 1987).

3.2.2 Harmonic Bifurcation

A real eigenvalue of $\mu_\ell = 1$ indicates a harmonic bifurcation (Ruelle, 1989). This eigenvalue represents an eigenvector that rotates 360° in one cycle and therefore does not change; this implies that the new periodic solution will have the same period as the old one. In fact, two new periodic solutions bifurcate from the old solution (Sparrow, 1982; Feldstein, 1987).

3.2.3 Toral Bifurcation

A toral or diffeo-Hopf bifurcation occurs when a complex conjugate pair of eigenvalues has magnitude one. Here, $\mu_\ell = \exp(i2\pi\theta)$, $0 < \theta \leq 1$, and θ can be rational or irrational. If θ is rational and $\theta \neq 1, 1/2, 1/3$, or $1/4$ (Iooss and Joseph, 1980; Guckenheimer and Holmes, 1983), then the resulting solution is a periodic one residing on the surface of a two-torus. If θ is irrational, then the orbit covers the surface of a two-torus and is called quasi-periodic.

Quasi-periodic solutions or tori are expected to appear in many routes to chaos (Nese, 1987). As shown by Wells and Shirer (1987), tori can connect two periodic solutions, such as P_m and P_j , of

different horizontal wavenumber. The corresponding bifurcation diagram takes on a goal form as in steady convection (Hirschberg, 1987). Therefore, exciting two wavenumbers one after the other by increasing the forcing rate in a fluid may lead to toral solutions (Figure 6a).

The above bifurcations are straightforward to track by following the changes in magnitudes of the eigenvalues. Even unstable periodic solutions in the sixteen-coefficient model can be traced if the instability originates from an eigenvalue of the 9x9 submatrix D in (3.6). In the next chapter, we will use these ideas to investigate whether toral bifurcations can occur in thermohaline convection.

Chapter 4

PHYSICAL INTERPRETATION OF MODEL SOLUTIONS

We begin integrating the model for values of $Ra_T > H_k$ as discussed in Chapter 2. The results of these integrations give stable steady or periodic solutions. By examining the stability of these solutions, we can determine when toral solutions bifurcate from the periodic ones and whether these new toral solutions are stable or unstable. In this chapter, specific solutions for realistic parameter values are examined to determine the changes in density, temperature and salinity characterizing these solutions. In particular, we focus on the changes in the background profiles of density.

4.1 Bifurcation Diagrams Representing Model Solutions

To construct bifurcation diagrams for particular values of Ra_S and a that show the steady and periodic solutions of the model, we find the periodic branches numerically, while we determine the steady solutions analytically. To find the forcing rates yielding toral solutions, we begin integrating the model using values of Ra_S and Ra_T that are just past those for the bifurcation points H_m and H_j ; these integrations give the P_m and P_j branches, as shown in Figure 6a.

Using the eigenvalue analysis discussed in Chapter 3, we look for diffeo-Hopf bifurcation points on both the P_m and P_j branches; as we noted in Section 3.2.3, these bifurcation points signal the existence of toral branches.

Diffeo-Hopf points emanate from the double Hopf point on the conductive solution as P_m and P_j are separated. These points are denoted D_j on Figures 7 and 8. Since the steady convective solutions S_m and S_j generally have large basins of attraction, we would like to move the periodic branches and diffeo-Hopf points as close as possible to the steady regular turning points F_m and F_j , where the basins of attraction for S_m and S_j are the smallest and the basin for the toral solution is the largest, provided the toral solution is stable.

Reducing the basins of attraction for the steady solutions S_m and S_j can be achieved by making the value of H_{mj} less than that of both F_m and F_j , which are the minimum values of Re_T for the steady solutions to the models V_m and V_j , respectively (Figures 7 and 8).

The equation describing the steady states can be calculated by setting the temporal derivatives of the five-component V_k model, $k =$

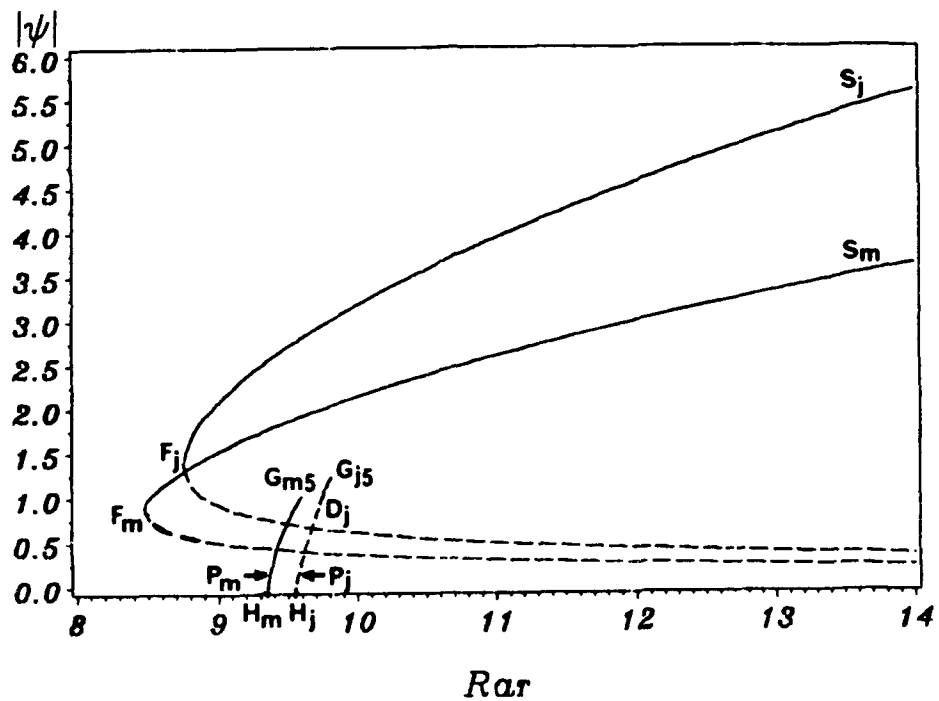


Figure 7 Bifurcation diagram for $Re_S=1.6836$, $a=0.486$, $m=2$, $j=1$, $P=7$ and $\tau=0.01$. Hopf and diffeo-Hopf bifurcation points are denoted by H_k and D_j , respectively, where $k=m$ or j . Here, G_{m5} and G_{j5} represent periodic regular turning points on the periodic branches P_m and P_j , and F_m and F_j are steady regular turning points on the steady branches S_m and S_j . There is no stable secondary branch S_{mj} . Solid curves represent stable solutions, and dashed curves denote unstable ones.

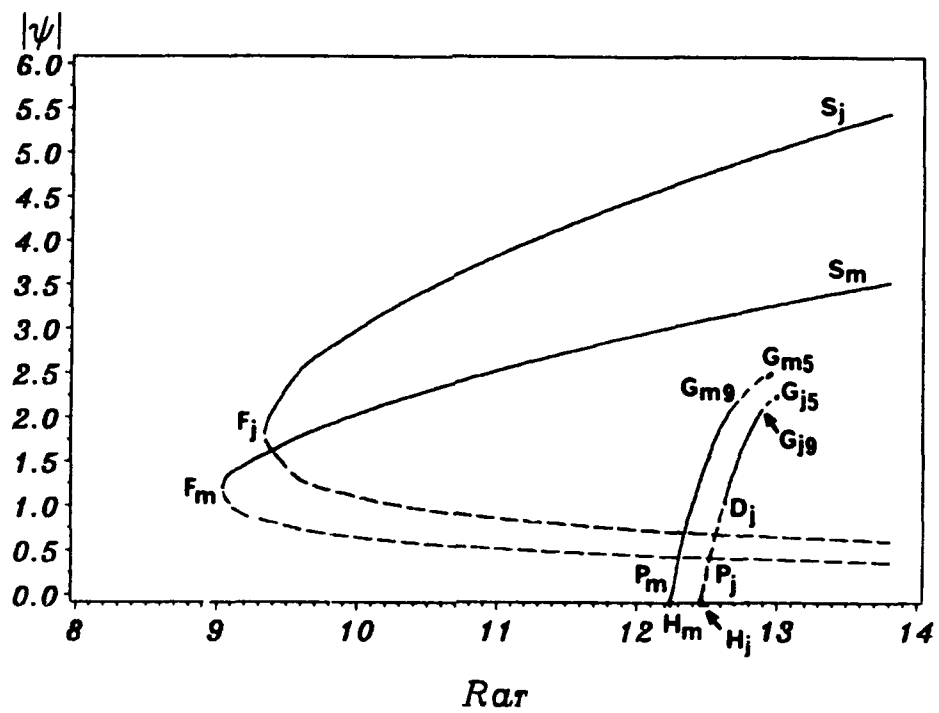


Figure 8 Bifurcation diagram for $Ra_S=5.0$, $a=0.486$, $m=2$, $j=1$, $P=7$ and $\tau=0.01$. Hopf and diffeo-Hopf bifurcation points are denoted by H_k and D_j , respectively, where $k=m$ or j . Here, G_{m5} and G_{j5} represent periodic regular turning points on the periodic branches P_m and P_j , and F_m and F_j are steady regular turning points on the steady branches S_m and S_j . There is no stable secondary branch S_{mj} . New bifurcation points are the harmonic ones G_{m9} and G_{j9} on P_m and P_j . Solid curves represent stable solutions, and dashed curves denote unstable ones.

m or j , to zero and then by manipulating the remaining terms to produce a quadratic in γ_{k1}^2 :

$$\gamma_{k1}^4 k^3 a^3 \xi^2 + \gamma_{k1}^2 [8\xi^3 a k \tau^2 + 8\xi^3 a k - 8a^3 Ra_T k^3 + 8a^3 k^3 \tau Ra_S] +$$

$$64\xi^4 \tau^2 / a k - 64aRa_T k \tau^2 \xi + 64\tau a Ra_S k \xi = 0 , \quad (4.1)$$

where $\xi = k^2 a^2 + 1$. This equation gives the parabolic curves that represent the m and j steady solutions, S_m and S_j (Figures 7 and 8).

To obtain the value of Ra_T at F_k , we make the discriminant of (4.1) vanish and solve for $Ra_T(F_k)$:

$$Ra_T(F_k) = \left\{ (\tau Ra_S)^{1/2} + \left[\frac{(1-\tau^2)(k^2 a^2 + 1)^3}{k^2 a^2} \right]^{1/2} \right\}^2 . \quad (4.2)$$

Requiring that $|Ra_T(H_{mj})| < |Ra_T(F_k)|$ for both $k = m$ and $k = j$ produces a quadratic inequality in Ra_S having a double root. It is interesting to note that using the approximate formula (2.48) for H_k instead of the exact one (2.47) gives poor results. Therefore, use of the full Hopf equation (2.47) is necessary to produce the correct values. For $m = 2$, $j = 1$, $a = a_{mj} = 0.49343$, and $Ra_S = 1.6836$, we find that H_{mj} , F_m , and F_j all coincide; however, $Ra_T(H_{mj}) < F_m$ or F_j is not possible for any values of the parameters. Thus, we conclude that $Ra_S = 1.6836$ is the best value of the forcing rate that yields

values of H_m and H_j that are as close to F_m and F_j as possible when the value of a is varied from a_{mj} . When the magnitude of the aspect ratio is chosen to be slightly smaller than that of a_{mj} (as in Figures 7 and 8, where $a = 0.486$), H_{mj} separates into H_m and H_j , and these points move to larger values of Ra_T . Also, F_m and F_j separate so that $Ra_T(F_m) < Ra_T(F_j)$ for $a < a_{mj}$. The result is that the steady regular turning points always occur at smaller values of Ra_T than the Hopf points when $a \neq a_{mj}$.

The dashed lower branches of the steady curves in Figures 7 and 8 are unstable. However, from an eigenvalue analysis of the steady solutions, we find that both upper branches are stable in the sixteen-coefficient model. For the branch S_j to be stable, even when it bifurcates from the conductive solution at larger values of Ra_T than does S_m , there must be a bifurcation point on the unstable branch of the j steady solution (e.g. Laufersweiler, 1987; Hirschberg, 1987). Here, an eigenvalue μ_m , is equal to one.

This deduction can be seen by tracing the eigenvalues on the steady solutions (Figure 6b). We note that the magnitudes of all the characteristic multipliers will be less than one on a stable steady solution, but at least one multiplier has magnitude greater than one

on an unstable solution; moreover, these magnitudes vary continuously. To trace these eigenvalues, we consider a case without Hopf bifurcations and begin on the stable conductive solution before the steady bifurcation points (Figure 6b). Here, all eigenvalues have magnitude less than one, since both the m and j conductive solutions are stable. Then, we follow a particular steady solution, m or j , noting that an eigenvalue will have magnitude one at a bifurcation point and the steady regular turning points F_k (cf. Figures 6b, 7 and 8).

Since both upper branches are stable in the sixteen-coefficient model, all sixteen eigenvalues have magnitude less than one on these solutions. This is found by treating the steady solutions as periodic ones, and performing an eigenvalue analysis. It is not possible for the S_j branch to be stable unless the eigenvalue μ_m , which became greater than one at the m steady bifurcation point, becomes less than one before F_j . Therefore, there must be a bifurcation point somewhere on the unstable branch of S_j at which $\mu_m=1$. This secondary steady bifurcation may produce an unstable secondary branch connecting the m and j steady solutions; as noted by Chang and Shirer (1984), such connecting branches are commonly found in convective flows.

As we can see from Figure 7, there are several striking characteristics of the periodic solutions. First, as signalled by the occurrence of an eigenvalue equal to one in the V_m and V_j models, the P_m and P_j branches end suddenly via periodic regular turning points G_{k5} , $k = m$ or j (Figure 9a). This bifurcation is not a stable harmonic one since no periodic solution replacing P_m can be found if the model is integrated for values of $Ra_T > G_{k5}$; the preferred solution becomes the steady one, S_k , depending on the periodic branch near which the model was initialized.

The second important characteristic of Figure 7 is the absence of a connecting secondary branch indicating the existence of a stable toral solution. A diffeo-Hopf point D_j is found only on the P_j branch; at this point the periodic solution gains stability. This toral bifurcation is important since in its absence, there would be no stable P_j solution. Near D_j , any energy put into the $(m,1)$, $(m+j,2)$, $(m-j,2)$, and $(0,4)$ wavenumbers quickly decays. Since no D_m bifurcation point exists on P_m , there can be no connecting branch to provide an exchange of stability between periodic solutions of wavenumber m and those of wavenumber j .

As the forcing rate owing to salinity is varied from $Ra_S =$

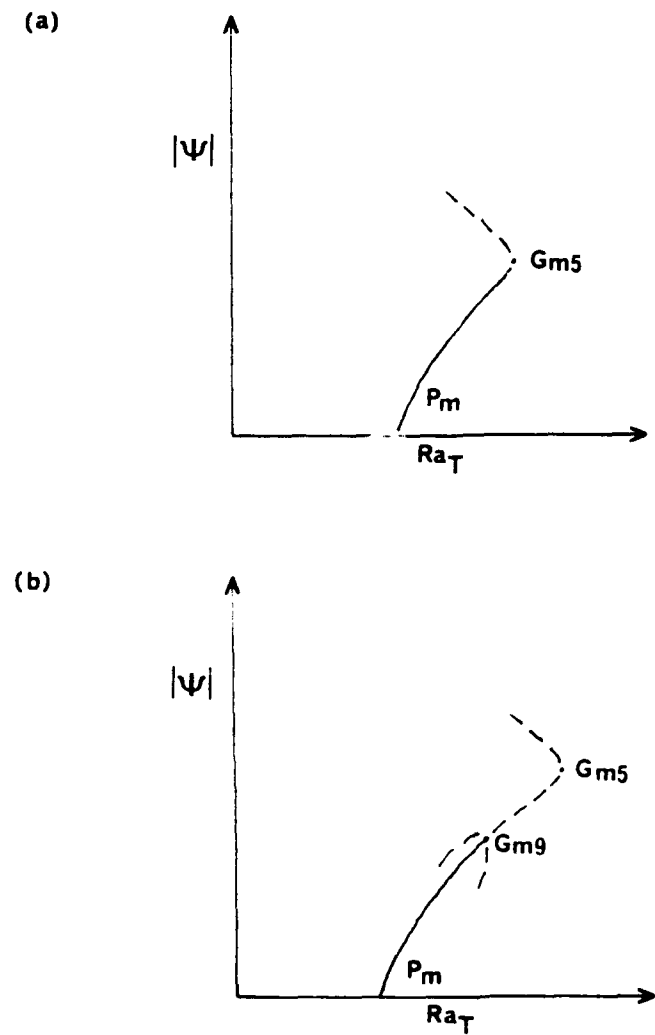


Figure 9 A schematic depiction of the periodic branch P_m in (a) the five-coefficient model and in (b) the sixteen-coefficient model. At the periodic regular turning point G_{m5} , the stable periodic solution (solid) turns towards smaller values of Ra_T and becomes unstable (dashed). At the harmonic bifurcation point G_{m9} , the periodic solution becomes unstable owing to excitation of some of the other 11 modes.

1.6836 to $Ra_S = 5.0$ (Figures 7 and 8), the Hopf bifurcation points move to larger values of Ra_T , and all solutions extend to larger values of $|\psi_{k_1}|$. Characteristics similar to those seen in Figure 7 are found at this larger value of Ra_S , with the addition of harmonic bifurcation points G_{m9} and G_{j9} on P_m and P_j (Figures 8 and 9b). From an eigenvalue analysis, we find that near $Ra_T = 12.65$ and $Ra_T = 12.75$, an eigenvalue from each of the 9x9 m and j submatrices is real and has magnitude one. Numerical evidence supporting the occurrence of a harmonic bifurcation near the end of P_m for $Ra_S = 5.0$ is shown in Table 1 in Chapter 3. Near the end of P_m at $Ra_T = 12.8$, there is an eigenvalue approaching one, namely μ_1 . The other multiplier μ_2 having a value near one indicates integration for one period. We recall that $\mu_k = 1$ can imply several things: (1) a harmonic bifurcation, (2) a periodic turning point, and (3) integration for one period. It is sufficient to note that these harmonic bifurcations exist and that they produce unstable periodic solutions (Figure 9b); they are not explored further here since these bifurcations do not indicate toral solutions.

Keeping the same value of Ra_S as in Figure 7, and varying the magnitude of a , we can see how the locations of the Hopf bifurcation

points H_m and H_j , the harmonic bifurcation points G_{k_9} , the periodic turning points G_{k_5} , and the diffeo-Hopf points D_j and D_m change on P_m and P_j (Figure 10). We find that the H_m (large dots on curve) and H_j (solid curve) curves intersect to create H_{mj} at $a_{mj} \approx 0.49343$, as calculated from (2.49). Parallel to these Hopf curves are the curves for the periodic turning points G_{ms} (small dot) and G_{js} (large dash) that represent the ends of the periodic branches. These curves also intersect at a_{mj} , indicating that the periodic branches end at the same value of Ra_T . As the branches are separated, the G_{k_5} lines also separate; the end of the j branch becomes farther from that of the m branch when $a < a_{mj}$. The reverse is true for $a > a_{mj}$.

From Figure 10, we find that there are only single diffeo-Hopf lines on each side of a_{mj} : D_j (small dash) on P_j when $a < a_{mj}$, and D_m (dash dot) on P_m when $a > a_{mj}$. In both cases, the diffeo-Hopf points occur on the periodic solution that branches second from the conductive solution. For a stable toral solution, as occurs in rotating convection (Wells and Shirer, 1987), a sufficient condition is that both diffeo-Hopf curves occur to the right of a_{mj} with D_m before D_j , or the left of a_{mj} with D_j before D_m . With only a single curve of diffeo-Hopf points on one side of a_{mj} for a given Ra_S , we

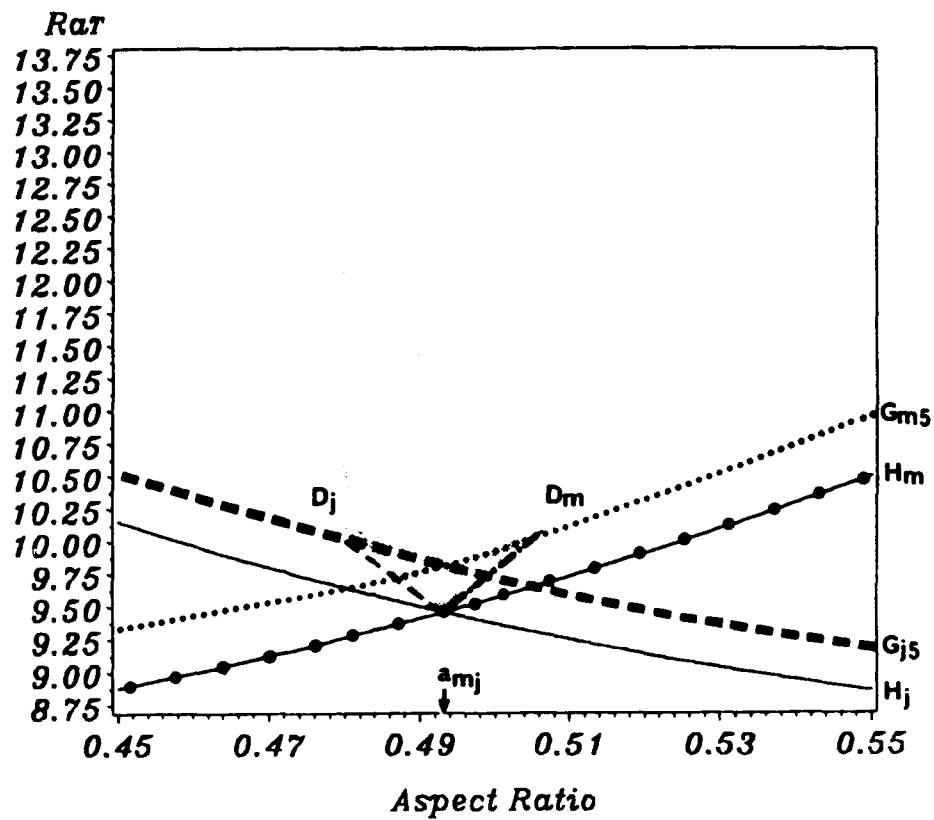


Figure 10 Variation of the values of the bifurcation points with aspect ratio when $Ra_S = 1.6836$, $m=2$, $j=1$, $P=7$ and $\tau=0.01$.

The periodic solutions grow from the conductive solution at H_m (curve through large dots) and H_j (solid) and end at the periodic regular turning points G_m5 (small dots) and G_j5 (large dash). The unstable toral region (shaded) begins at the diffeo-Hopf points D_m (dash dot) and D_j (small dash) and extends toward larger values of Ra_T ; the actual edge of this region is not known.

see that the toral solution is unstable. If the diffeo-Hopf points were to occur on the first branching periodic solution, then the toral solution would be stable. This would occur if the curve for D_m sloped to the left rather than to the right of a_{mj} . Thus, by knowing the slope of these diffeo-Hopf curves at $a = a_{mj}$ and then by comparing them to the slopes for the Hopf curves, we can infer the stability information of the branching quasi-periodic solutions in the entire toral region.

At $Ra_S = 5.0$ (Figure 11), the H_m , H_j , G_{ks} , and D_j curves are similar to those for the case $Ra_S = 1.6836$ in Figure 10. Now, there are two additional curves representing the harmonic bifurcations G_{ms} (small dots on curve) and G_{js} (long dash), at which the periodic branches lose stability. As the magnitude of Ra_S is increased, changes in the size of the toral region depend on how far D_j is from H_j , and also on how far D_m is from H_m , or equivalently on the distance D_j and D_m have moved up the periodic branches. In the range of $Ra_S = 1.6836$ to $Ra_S = 65.0$, the size of the unstable toral region remains about constant, since the value of $|\psi_{k_1}|$ at D_j in this range of Ra_S is about constant at $|\psi_{k_1}| \approx 1.2$ (Figures 7, 8 and 12). The size of the toral region also depends of the range of a , since at

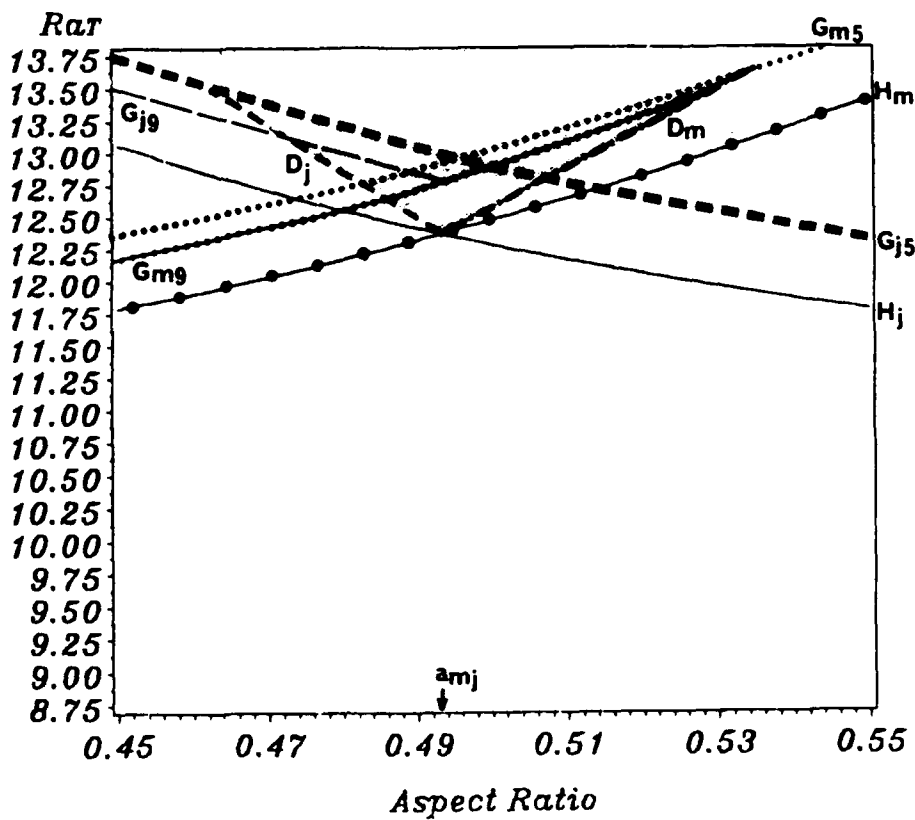


Figure 11 Variation of the values of the bifurcation points with aspect ratio when $Ra_S=5.0$, $m=2$, $j=1$, $P=7$, and $\tau=0.01$. The periodic solutions P_m and P_j grow from the conductive solution at H_m (curve through large dots) and H_j (solid), lose stability, or gain a positive characteristic multiplier if already unstable, at G_{m9} (curve through small dots) and G_{j9} (long, thin dash), and end at the periodic regular turning points G_{m5} (small dots) and G_{j5} (large dash). The unstable toral region (shaded) begins at the diffeo-Hopf points D_m (dash dot) and D_j (small dash) and extends to larger values of Ra_T ; the actual edge of this region is not known.

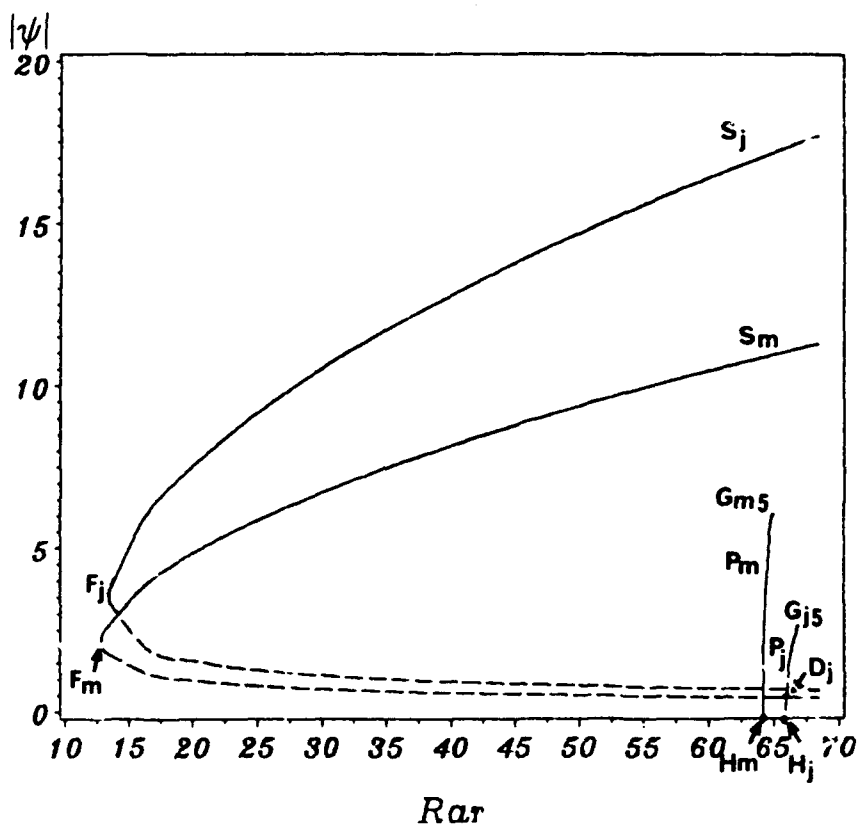


Figure 12 Bifurcation diagram for $Ra_g=65$, $a=0.486$, $m=2$, $j=1$, $P=7$ and $\tau=0.01$, corresponding to the melting sea ice case. Hopf and diffeo-Hopf bifurcation points are denoted by H_k and D_j , respectively, where $k=m$ or j . Here, G_{m5} and G_{j5} represent periodic regular turning points on the periodic branches P_m and P_j , and F_m and F_j are steady regular turning points on the steady branches S_m and S_j . There is no stable secondary branch S_{mj} . Solid curves represent stable solutions, and dashed curves denote unstable ones.

larger values of Ra_S , the D_m and D_j curves extend to larger values of

a. The regions of unstable tori are shaded in Figures 10 and 11.

For the values of $Ra_S \leq 65.0$ that have been investigated, we have not found any stable tori, apparently implying that stable toral solutions do not characterize double diffusive convection. We can conclude that the existence of a double Hopf point does not always guarantee the existence of stable tori for nearby values of a , but it does imply that there will be either stable or unstable tori.

Although the values of Ra_T and Ra_S used in Figures 10 and 11 give steady and periodic solutions, the values of the forcing rates are far from the realistic ones represented by the $Ra_S = Ra_T$ line of Figure 3. Using these aphysical values $Ra_S = 1.6836$ and $Ra_T = 9.7$ of the forcing rates produces an unrealistic background density profile. This is evident in the steady solution shown in Figure 13.

Since toral solutions involve the S_{04} and T_{04} terms of the modifications of the background salinity and temperature profiles, and since the toral solutions are unstable, these terms are not activated. Thus the modifications of background density profiles can be expressed exclusively in terms of the T_{02} and S_{02} coefficients.

Although the background temperature and salinity modifications

$S_{02} \sin(2z)$ and $T_{02} \sin(2z)$ from the Fourier expansions of S^* and T^*

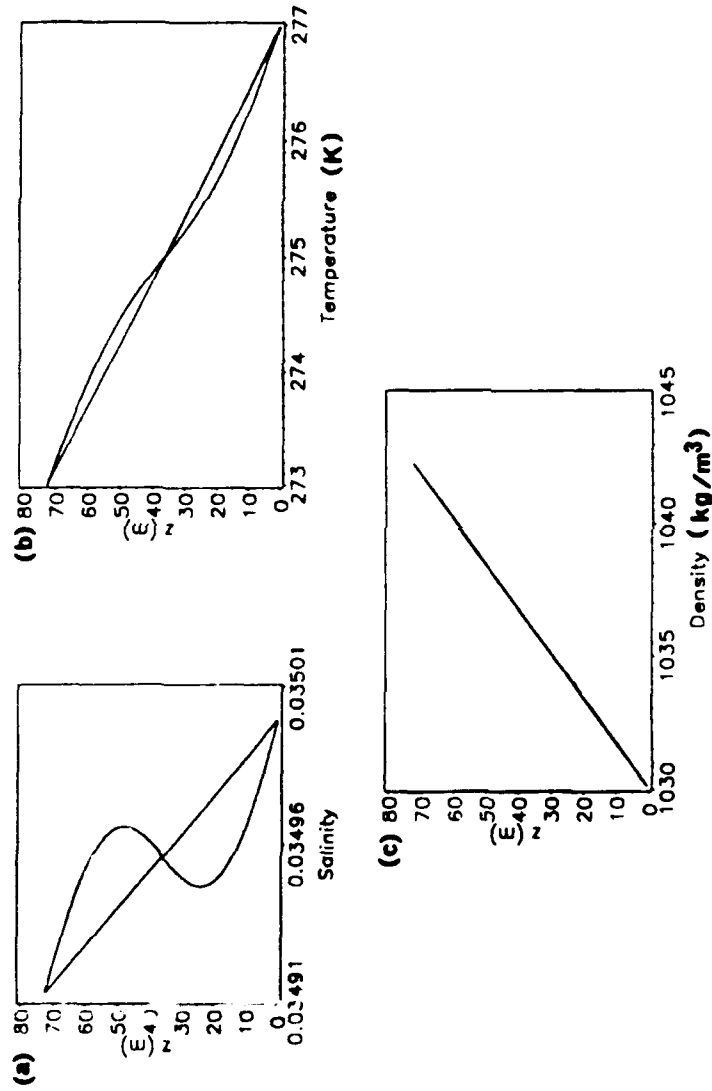


Figure 13 Background profiles (lines) and modification of the background profiles (curves) for salinity (a), temperature (b), and density (c) as functions of depth when $Ra_g=1.6836$, $Ra_T=9.7$, $a=0.486$, $m=2$, $j=1$, $P=7$ and $\tau=0.01$ for steady solution S_m . The fact that Ra_g and Ra_T are different in magnitude produces the aphysical density profile.

act to decrease the interior gradients as expected, the background density profile does not become constant with height because the addition of $\rho_{02} \sin(2z)$ to $\rho_{00} + \rho_0(z)$ is negligible (Figure 13c). Because of the fact that $Ra_T \gg Ra_S$, which corresponds to a large amount of heating from below destabilizing the system, the background density increases rapidly with height. This shows that straying only somewhat from the constant density line (Figure 3) can lead to unphysical solutions.

After being cautioned as to the care required in choosing values of Ra_S and Ra_T , we would like to know physically why the P_m and P_j solutions exist, why the steady solution is preferred, and why the periodic solutions end abruptly. These topics are discussed in the next section.

4.2 Physical Interpretation of the Periodic and Steady Solutions

We begin by finding values of the parameters in the definitions (2.30) and (2.31) of Ra_S and Ra_T that satisfy the constant density relation $\beta\Delta S = \alpha\Delta T$. The density ratio $\alpha\Delta T/\beta\Delta S$ represents a very important observable parameter in the ocean. For example, large values of $\alpha\Delta T/\beta\Delta S$ imply a greater destabilization by heat than stabilization by salt. This density ratio will prove useful in

guiding our examination of thermohaline convection in estuaries and under melting sea ice.

4.2.1 Thermohaline Convection in Estuaries

Estuaries are areas of interaction between fresh and salty water, where a river current meets the ocean. Here, fresh water overrides salty water, which yields the desired salinity gradient for thermohaline convection. The large difference in salinity between the fresh and salty water produces a density gradient that drives a circulation. Although the density of the water depends on both temperature and salinity, in the estuary case, the temperature range is generally small (Dyer, 1973).

As an example, the longitudinal distributions of temperature and salinity in the Hardangerfjord in Norway are shown in Figure 14. In the winter, cool, fresh water overlies warm, salty water. Setting the salinity and temperature at the top equal to 33‰ and 5.5°C , and at the bottom to 35‰ and 6.5°C gives $\Delta S=2\text{‰}$ and $\Delta T=1^{\circ}\text{C}$. Also, we set $T_{00}=280\text{ K}$, and $S_{00}=35\text{‰}$. These values give $\alpha\Delta T/\beta\Delta S=6.25\times 10^{-2}$, which is far from one and the constant density line. Also, these parameter values give $\text{Ra}_S=4.024$ and $\text{Ra}_T=0.252$. However, these values of the forcing rates are well below those for the constant

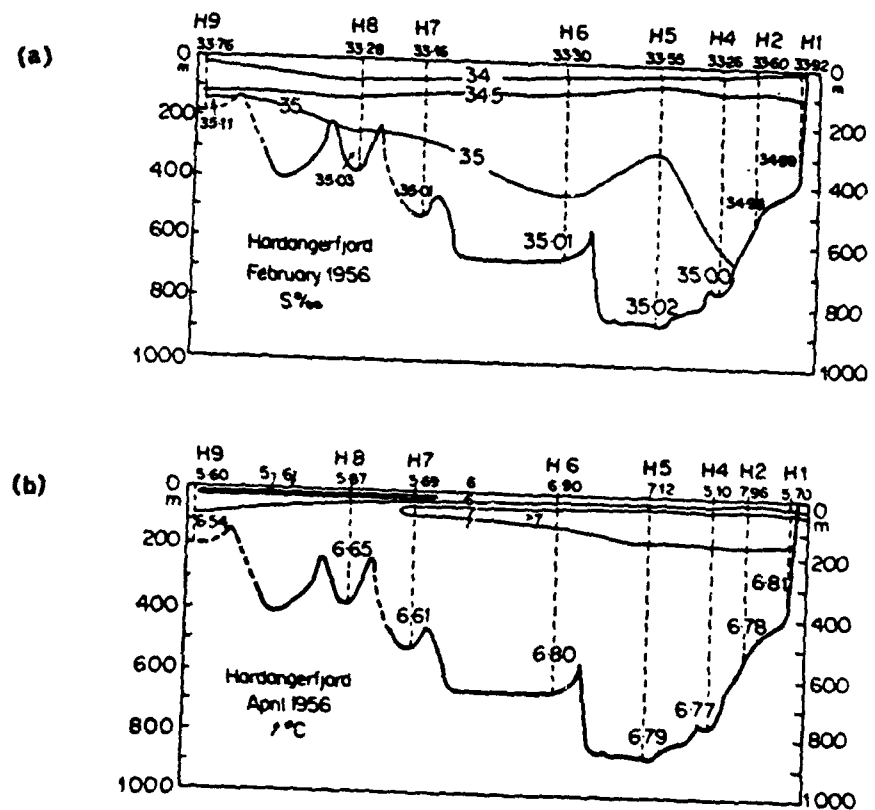


Figure 14 Winter distributions of salinity (a) and temperature (b) in a longitudinal section of Hardangerfjord, Norway (from Dyer, 1973).

density and Hopf lines in Figure 3, thereby indicating that a conductive solution would be stable. The salt gradient is so stabilizing that convection cannot occur. We conclude that the wintertime estuary case does not yield thermohaline convection.

4.2.2 Thermohaline Convection Under Melting Sea Ice

Melting sea ice provides a flux of fresh water to the surface layer of the ocean, possibly producing the desired salinity gradient for thermohaline convection. In order to have periodic solutions and a realistic background density, we choose the values of Ra_S near that for Ra_T and to the right of the intersection of the two curves in Figure 3. We will choose $Ra_S = 65.0$ and $Ra_T = 64.94$. The bifurcation diagram for $Ra_S = 65.0$ is shown in Figure 12, which is similar to the cases in Figures 7 and 8.

Upon knowing the values of the forcing rates, we find that choosing the parameter values for the sea ice case is quite straightforward. We choose $T_{00} = 283$ K, the temperature of the summertime polar seasonal thermocline (Figure 15c). The temperature at the top must be near that of melting ice, 277 K. Choosing a lower temperature is inconsistent with the linear equation of state (2.14)

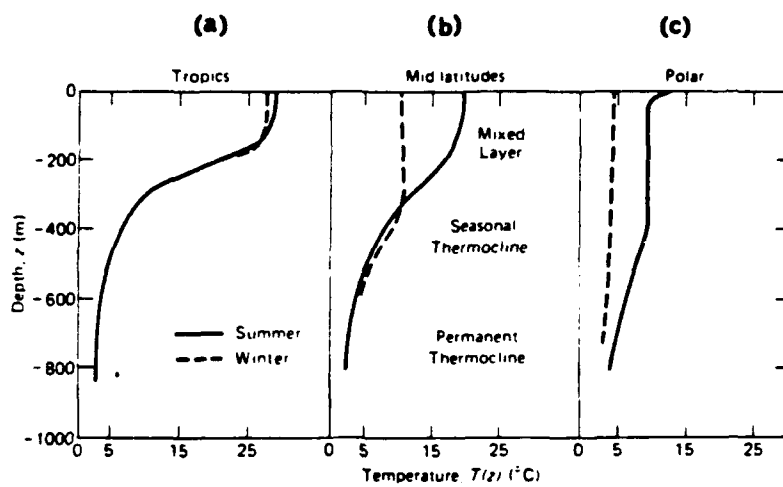


Figure 15 Schematic temperature distributions with depth for tropical (a), mid-latitude (b), and polar regions (c) for summer (solid) and winter (dashed) conditions. The major regimes in the vertical are the near-surface mixed layer, the seasonal thermocline, and the deep, permanent thermocline (from Apel, 1987).

used to develop the model. Thus, we obtain $\Delta T = 6$ K. As before, we specify $S_{00} = 35\%$.

In order to find the values of the other parameters and the magnitudes of the forcing rates from (2.30) and (2.31), we choose a value for ν . We note that for large-scale phenomena, the horizontal eddy diffusion term dominates (Table 2). However, on the convective scale $\nu_v \sim \nu_h \sim 100 \text{ m}^2/\text{s}$, which is the smallest value in the range of ν_h given in Table 2. Since $P = \nu/k_T$, we set $k_T = 14.286 \text{ m}^2/\text{s}$ in order to have $P = 7$.

Next, we must choose ΔS and z_T so that $\tilde{Ra}_S = \tilde{Ra}_T$. The value of ΔS for which $\Delta T/T_{00} \tilde{=} \Delta S/S_{00}$ is $\Delta S = 0.742\%$. When $\tilde{Ra}_T = 64.94$, we find from the value of ν and (2.31) that $z_T \approx 351.7 \text{ m}$. This depth agrees relatively well with that of the summer polar seasonal

Table 2 Typical values of horizontal and vertical eddy diffusion coefficients for large-scale motion of sea water (from Apel, 1987).

$$\nu_v = 3 \times 10^{-5} \text{ to } 2 \times 10^{-2} \text{ m}^2/\text{s}$$

$$\nu_h = 10^2 \text{ to } 10^5 \text{ m}^2/\text{s}$$

thermocline (Figure 15). Also, this depth is verified in Figure 16 by the location of the asterisk. Here, we combine (2.48) with (2.30) and (2.31) and let $a = a_{mj}$ to get

$$\frac{\Delta T}{T_{00}} = \frac{\Delta S}{S_{00}} \left[\frac{1}{1+\rho} \right] + \frac{(a_{mj}^2 m^2 + 1)^3}{a_{mj}^2 m^2} \left[\frac{\nu k_T \pi^4}{g z_T^3} \right]. \quad (4.4)$$

This equation gives values of z_T that are near the constant density line and the double Hopf point.

The spectral components for the periodic solution P_m for $Ra_S = 65.0$ and $Ra_T = 64.94$ are shown in Figure 17. We note that the salinity field (coefficients S_{m1} and S_{02}) lags the temperature field (coefficients T_{m1} and T_{02}) because of the differences in diffusivities represented by the ratio τ , as discussed in Chapter 2. However, to understand what the interaction between these components means physically, we must convert them to their dimensional forms using (2.21)-(2.26). Although the model gives numerical values for the temperature and salinity perturbations, it is difficult to explain the characteristics of the circulation unless T' and S' are combined to yield the perturbation density. Combining (2.15), (2.7), and (2.8), we find that

$$\rho_0 = -\Delta\rho - \frac{z}{z_T}, \quad (4.5)$$

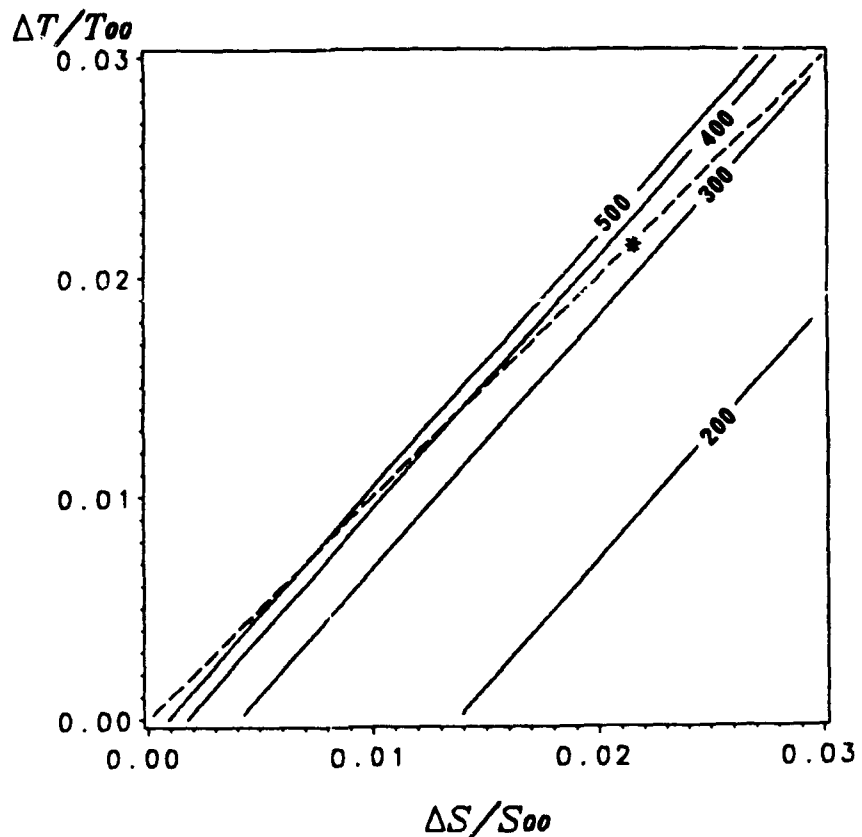


Figure 16 Values of domain depth z_T (m) for the double Hopf point with the following values: $K_T=14.286 \text{ m}^2/\text{s}$, $\nu=100 \text{ m}^2/\text{s}$, $P=7$, $T_{00}=283 \text{ K}$, $S_{00}=35\%$., $\Delta T=6 \text{ K}$, $\Delta S=0.742\%$., $m=2$, $j=1$, $g=9.8 \text{ m/s}^2$, and $a_{mj}=0.4934$. The constant density line is dashed, and the asterisk denotes the sea ice case discussed in the text.

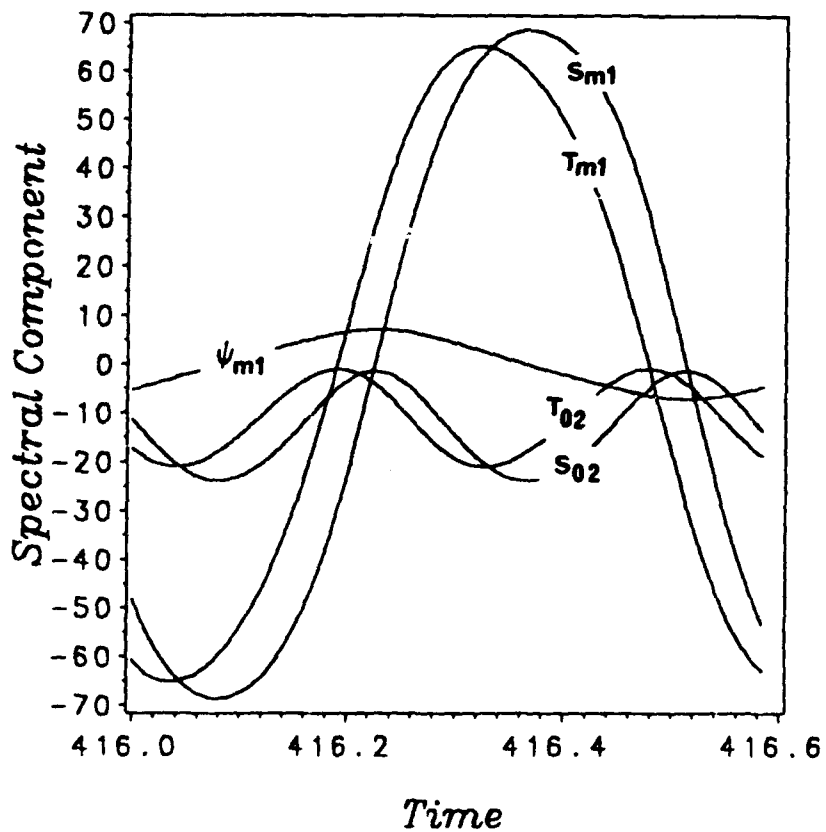


Figure 17 Variations in salinity coefficients S_{m1} and S_{02} , temperature coefficients T_{m1} and T_{02} , and stream function coefficient ψ_{m1} for the periodic solution P_m in the Veronis model for values of $Ra_S=65$, $Ra_T=64.94$, $a=0.486$, $P=7$, $\tau=0.01$, and $m=2$.

and

$$\frac{\Delta\rho}{\rho_{00}} = \frac{\Delta S}{S_{00}} - \frac{\Delta T}{T_{00}} . \quad (4.6)$$

Substituting $S_b' = S_{02}\sin(2z^*)$ and $T_b' = T_{02}\sin(2z^*)$, where b indicates the background state, into (2.16) gives

$$\frac{\rho_{02}}{\rho_{00}} = \frac{S_{02}}{S_{00}} - \frac{T_{02}}{T_{00}} , \quad (4.7)$$

where S_{02} and T_{02} are calculated from solutions to the model.

Substituting $S_c' = S_{m1}\cos(mx^*)\sin(z^*)$ and $T_c' = T_{m1}\cos(mx^*)\sin(z^*)$,

where c denotes the convective state, into (2.16) gives

$$\frac{\rho_{m1}}{\rho_{00}} = \frac{S_{m1}}{S_{00}} - \frac{T_{m1}}{T_{00}} , \quad (4.8)$$

where S_{m1} and T_{m1} are also calculated from the solutions.

The variations with time of the variables ρ_{m1} and ρ_{02} , along with $\overline{w'}$, are shown in Figure 18. Since $\overline{w'} > 0$, where the overbar denotes a horizontal average, implies an indirect circulation, for which more dense fluid is transported up and less dense fluid is brought down, we let $\rho_c' = \rho_{m1}\cos(mx^*)\sin(z^*)$ and $w' = mw_{m1}\cos(mx^*)\sin(z^*)$ to find that $\rho_{m1}w_{m1} > 0$ also implies an indirect circulation. From Figure 18, we see that the flow is

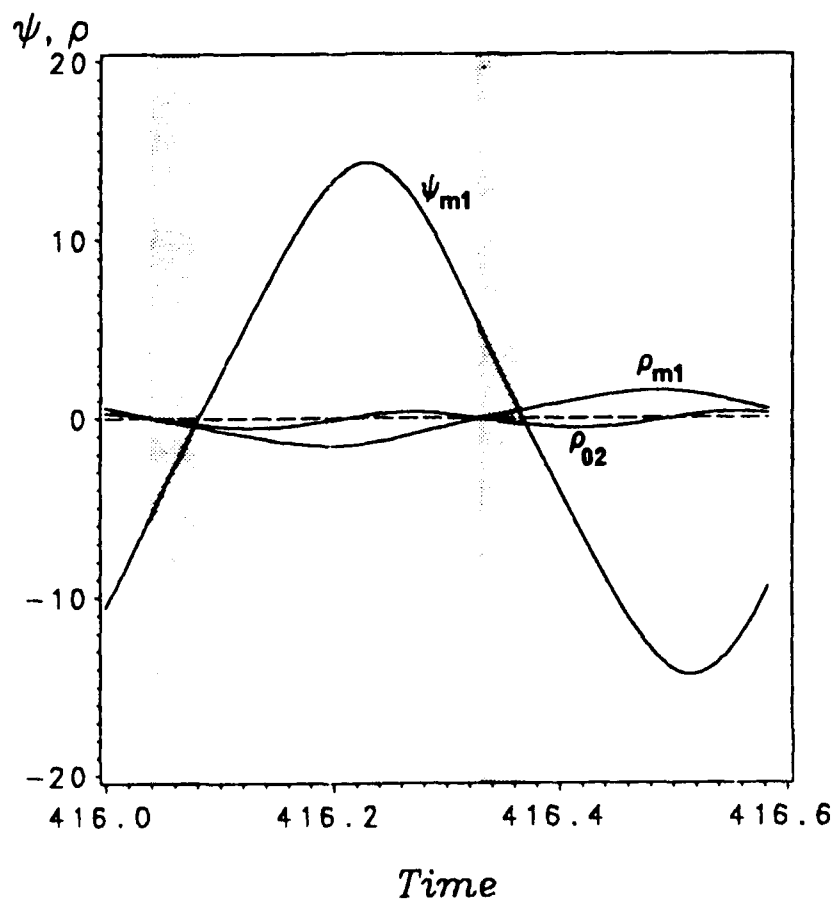


Figure 18 Variations in density coefficients ρ_{02} and ρ_{m1} and stream function coefficient ψ_{m1} corresponding to the periodic solution in Figure 17. The shaded area represents times in which the circulation is indirect.

characterized briefly by an indirect circulation between approximately $t = 416.04$ and $t = 416.08$, and again between approximately $t = 416.33$ and $t = 416.37$. This indirect circulation occurs for much less than half of the period. This behavior is similar to that seen in rotating convection (Pyle, 1986).

To examine the periodic solution in more detail, we contour the values of $\psi_C = \psi_{m1} \sin(mx^*) \sin(z^*)$ and $\rho'_C = \rho_{m1} \cos(mx^*) \sin(z^*)$ as functions of x^* and z^* , and we plot $\rho'_b = -\Delta\rho z/z_T + \rho_{02} \sin(2z^*)$ versus height (Figures 19a-19g) at various times throughout a single period (Figures 17 and 18). At $t = 416.00$ (Figure 19a), the circulation is direct, given by $\rho_{m1} \psi_{m1} < 0$: there is an upward transport of lighter fluid and a downward transport of heavier fluid. The background density increases with height implying static instability in the region of $0 < z^* < \pi/4$ and $3\pi/4 < z^* < \pi$, and the fluid responds by attempting to destroy these unstable gradients. The contribution to the total background density by $\Delta\rho$ in ρ_0 is negligible, since this case is almost on the constant density line.

Although less dense fluid is moving up, and there is a direct circulation, the stratification is unstable near the boundaries. The only way to eliminate the unstable density profiles at the boundaries is by having an indirect circulation ($\rho_{m1} \psi_{m1} > 0$) that moves more

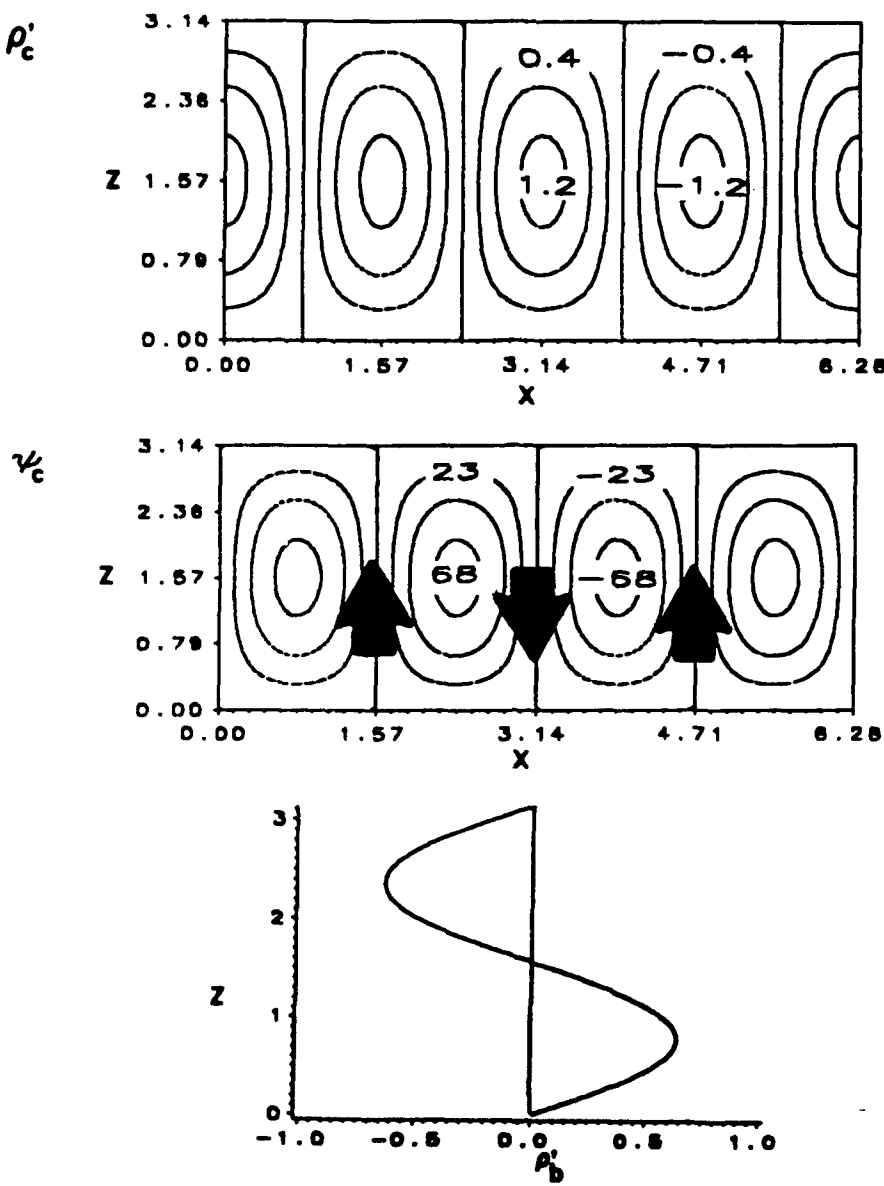


Figure 19 (a) Contours of convective density $\bar{\rho}_c$ (kg/m^3), stream function $\bar{\psi}_c$ (m^2/s), and the modification of the background density $\bar{\rho}_b$ (kg/m^3) for the periodic solution in Figure 18 (x and z are dimensionless). In (a), at time $t=416.00$, the circulation is direct since $\bar{\psi}_{m1}\bar{\rho}_{m1} < 0$, where $\bar{\psi}_{m1} < 0$ and $\bar{\rho}_{m1} > 0$. The background density profile is unstable near the boundaries because $\bar{\rho}_{02} > 0$.

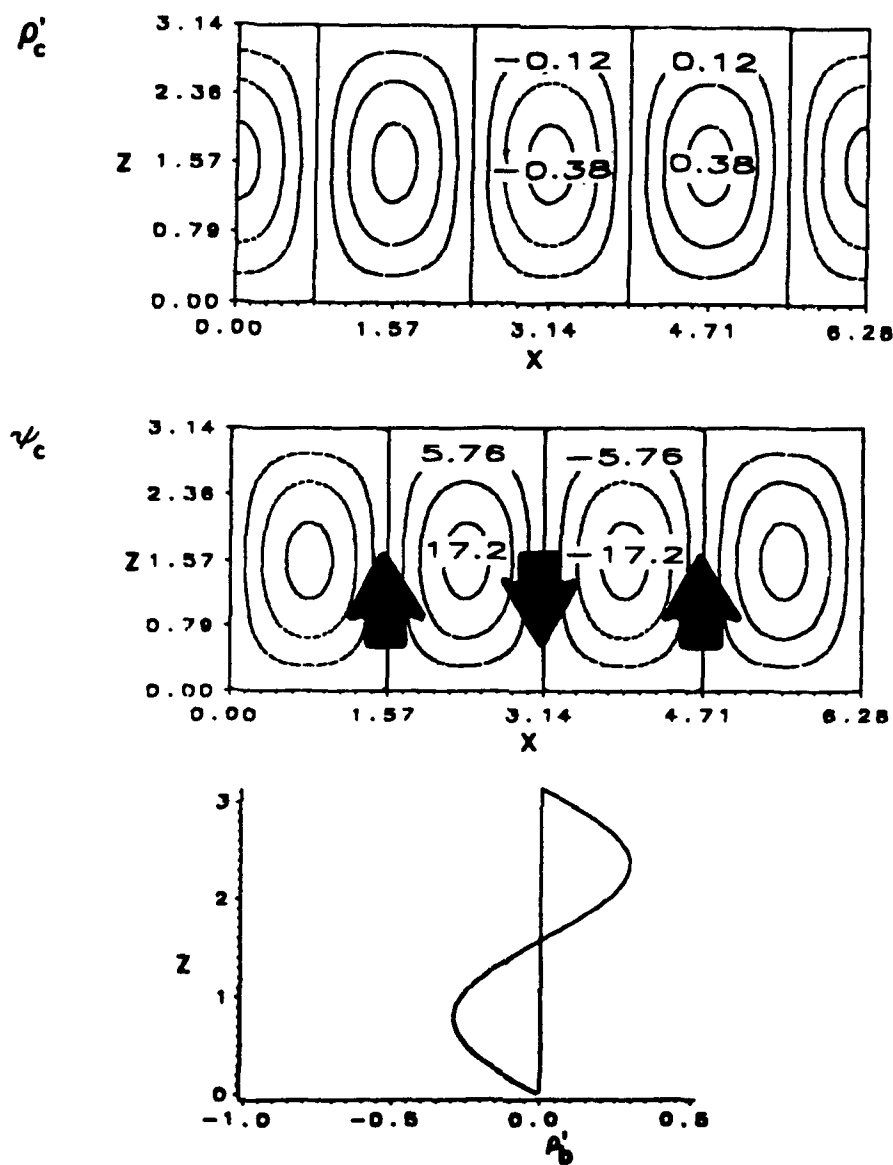


Figure 19 (cont.) (b) At time $t=416.06$, the circulation is indirect since $\psi_{m1}\rho_{m1} > 0$, where $\psi_{m1} < 0$ and $\rho_{m1} < 0$. The background density is unstable in the interior, because $\rho_{02} < 0$.

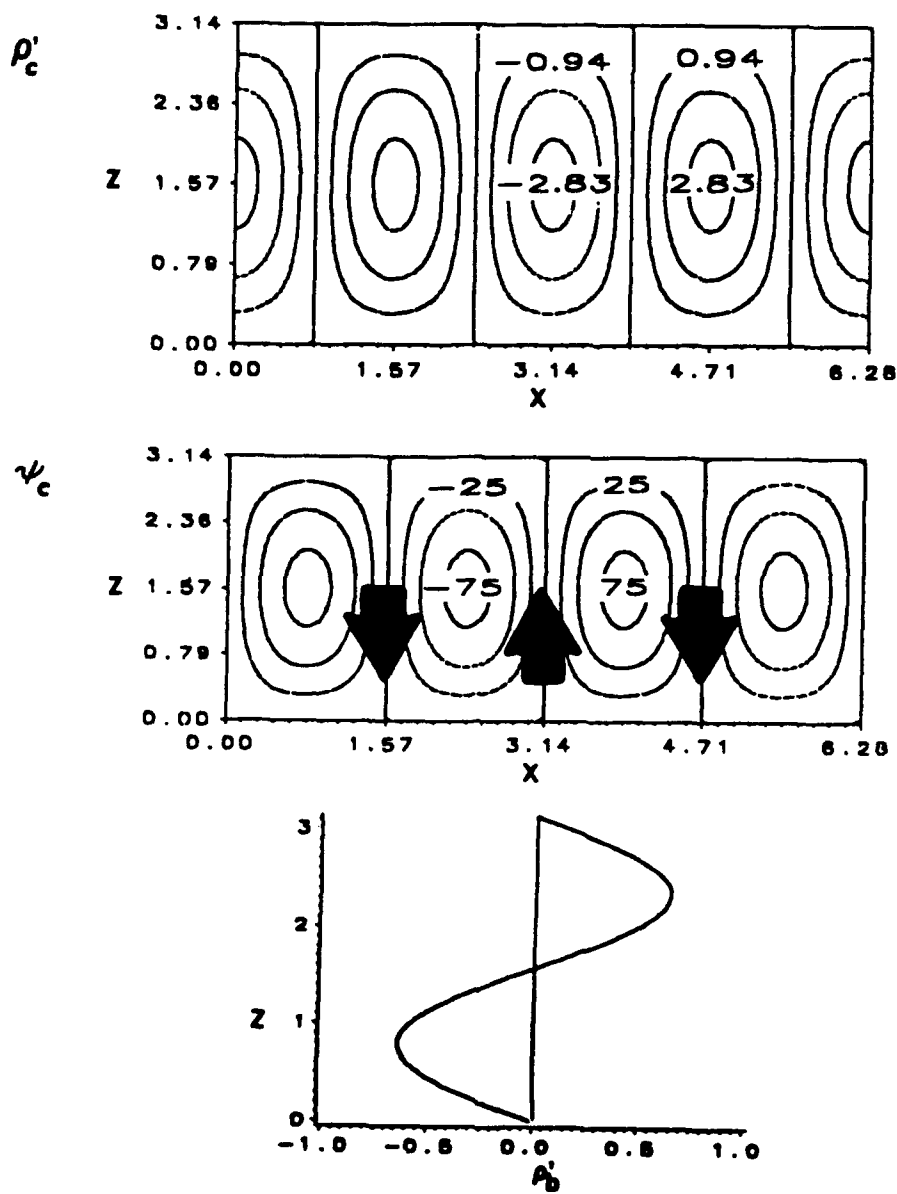


Figure 19 (cont.) (c) At time $t=416.18$, the circulation is again direct since ψ'_{m_1} has become positive and ρ'_{m_1} is still negative, and since the upward motion is in the center of the domain. The background density is still unstable in the interior.

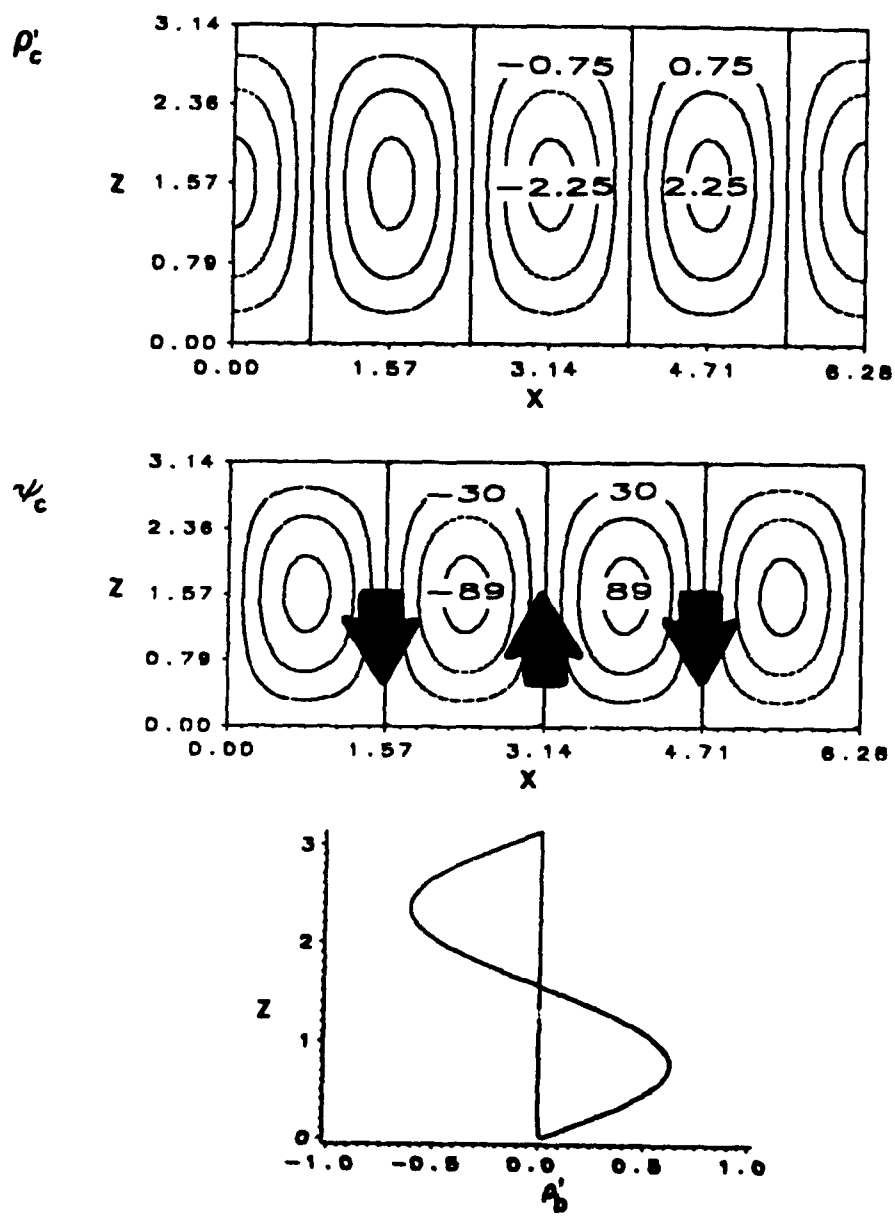


Figure 19 (cont.) (d) At time $t=416.25$, the circulation is direct since $\psi_{m1} > 0$ and $\rho_{m1} < 0$. Now, ρ_{02} has become positive, and the background density is again unstable at the boundaries.

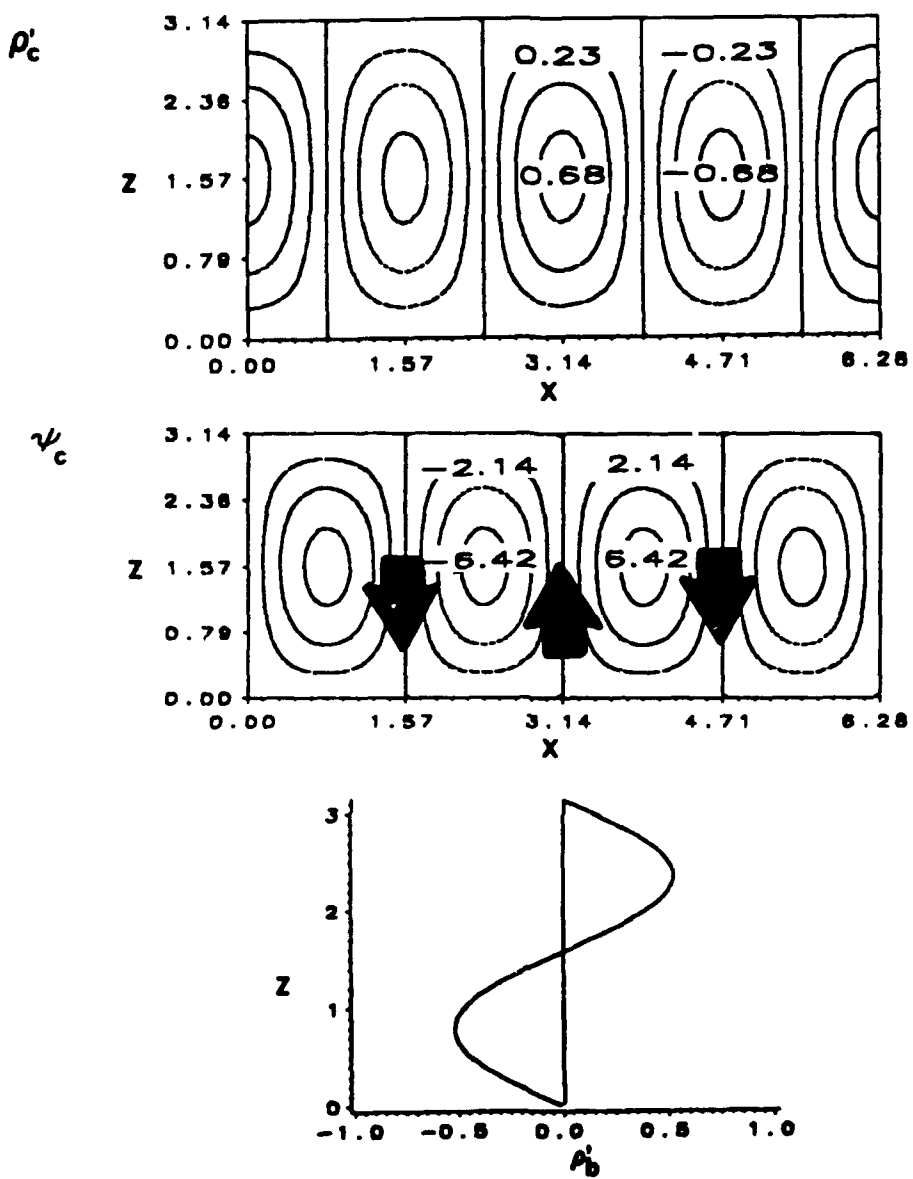


Figure 19 (cont.) (e) At time $t=416.36$, the circulation is indirect since ρ_{m1} has become positive. The background density is unstable in the interior as ρ_{02} is now negative.

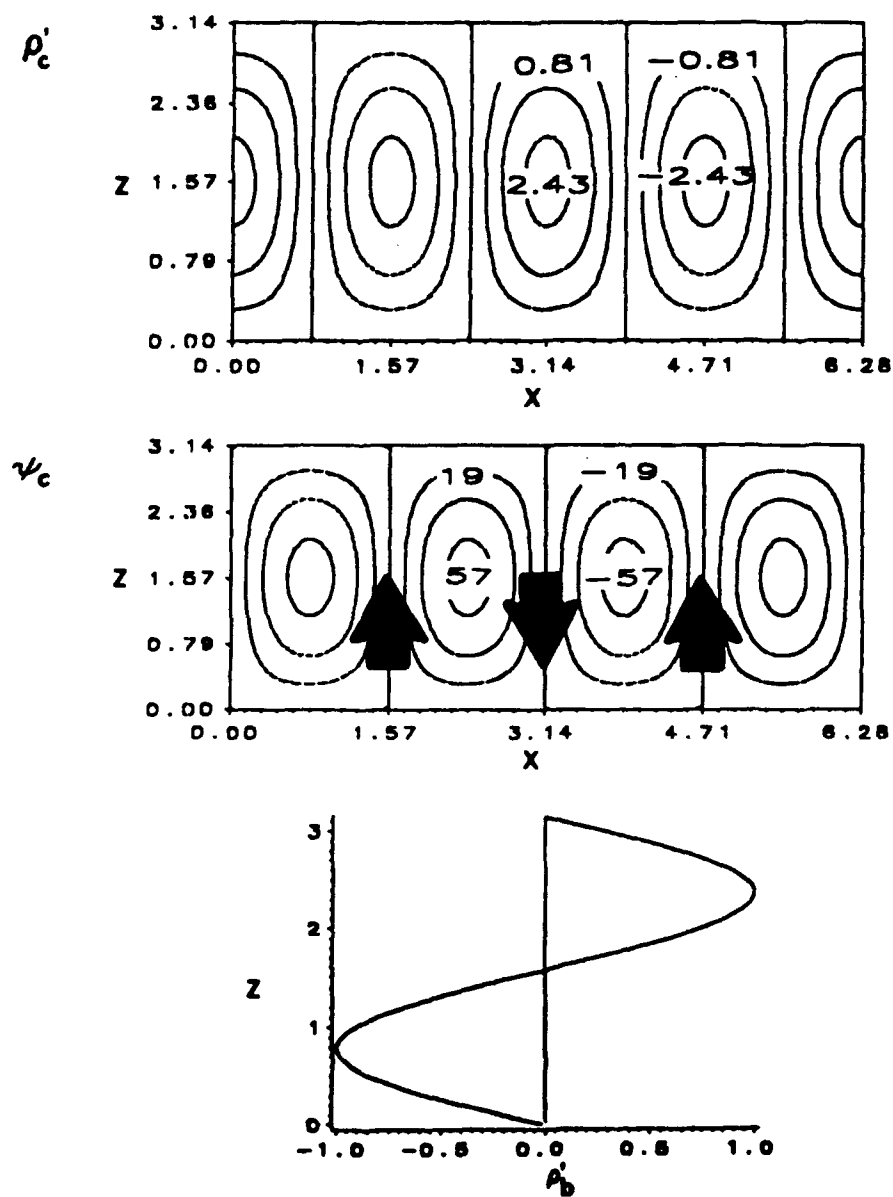


Figure 19 (cont.) (f) At time $t=416.44$, the circulation is direct since ψ_{m1} has become positive. Here, ρ_{02} is still negative, and the interior density gradient is unstable.

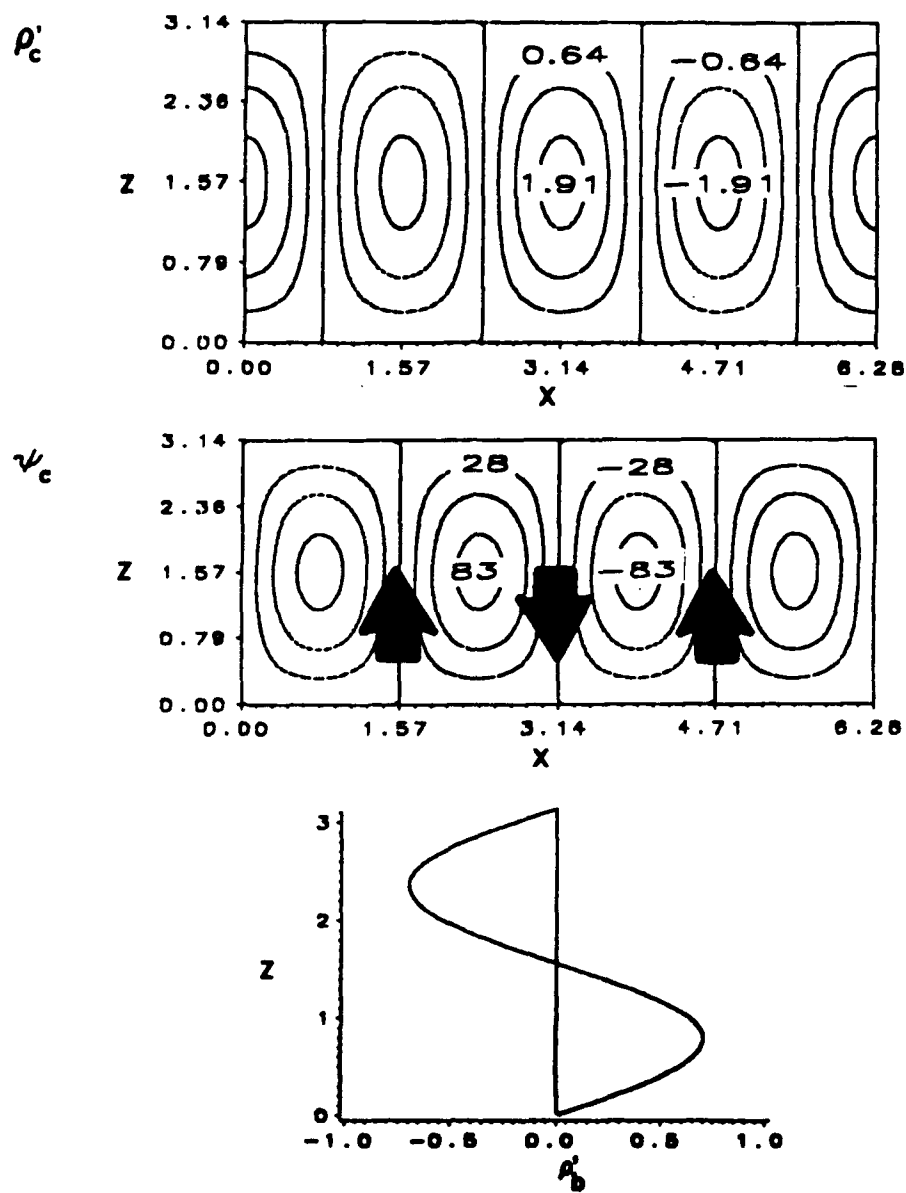


Figure 19 (cont.) (g) At time $t=416.55$, the circulation is direct, and the unstable density gradient is now near the boundaries.

dense fluid upwards (Figure 19b). This indirect circulation is short-lived since it creates another unstable gradient in the middle of the density profile that lasts longer than the indirect circulation. Note that the indirect circulation always occurs just after the value of ρ_{02} becomes negative (Figure 18), implying that an unstable interior density gradient occurs. Now, a direct circulation attempts to destroy this interior instability by bringing upwards lighter fluid that is created by the forcing from below (Figure 19c). This process is repeated in Figures 19e-g to complete the period.

The search for an equilibrium having no density variation with height produces a periodic solution, since an attempt to destroy an unstable gradient in one regime produces an unstable gradient in another. Eventually, this attempt to gain equilibrium breaks down as the amplitudes of the oscillations in the background modification become too large, and the flow can no longer create the necessary indirect circulations to maintain a periodic state. This breakdown occurs when the periodic branch ends, and the steady solution becomes the preferred one. The P_j solution, which becomes stable via the toral solution, has characteristics similar to those for the P_m solution.

The above behavior of the periodic solutions may be understood also by comparing the bifurcation diagrams in Figures 7, 8 and 12.

Here, the periodic solutions occur only at small values of $|\psi_{k_1}|$, so these solutions weakly transport heat and momentum vertically. As the value of the forcing rate is increased, greater vertical heat transport is required, which the oscillatory state cannot maintain, and so the periodic solution ends. The lower branch of the steady solution is probably unstable for the same reason. The stable steady solution provides the necessary large vertical transport of heat to maintain an equilibrium. Veronis (1968) found that for $P \geq 1$, the oscillatory solutions were replaced with steady solutions, that had larger heat fluxes.

An example of a steady solution S_m for the same Ra_S as in the periodic solution discussed above is shown in Figure 20. As before, the slope owing to $\Delta\rho$ is negligible, and the contribution from ρ_b' dominates in the background density profile. Here, the circulation is always a direct one that is trying to alter the background density gradient in the interior, where more dense fluid overlies less dense fluid, in order to create a background density profile that is constant with height. The steady solution does not accomplish this task because the forcing rates $Ra_S > 0$ and $Ra_T > 0$ produce a steady source of fresh water above and warm water below. This type of forcing produces less dense fluid at the boundaries, which can be

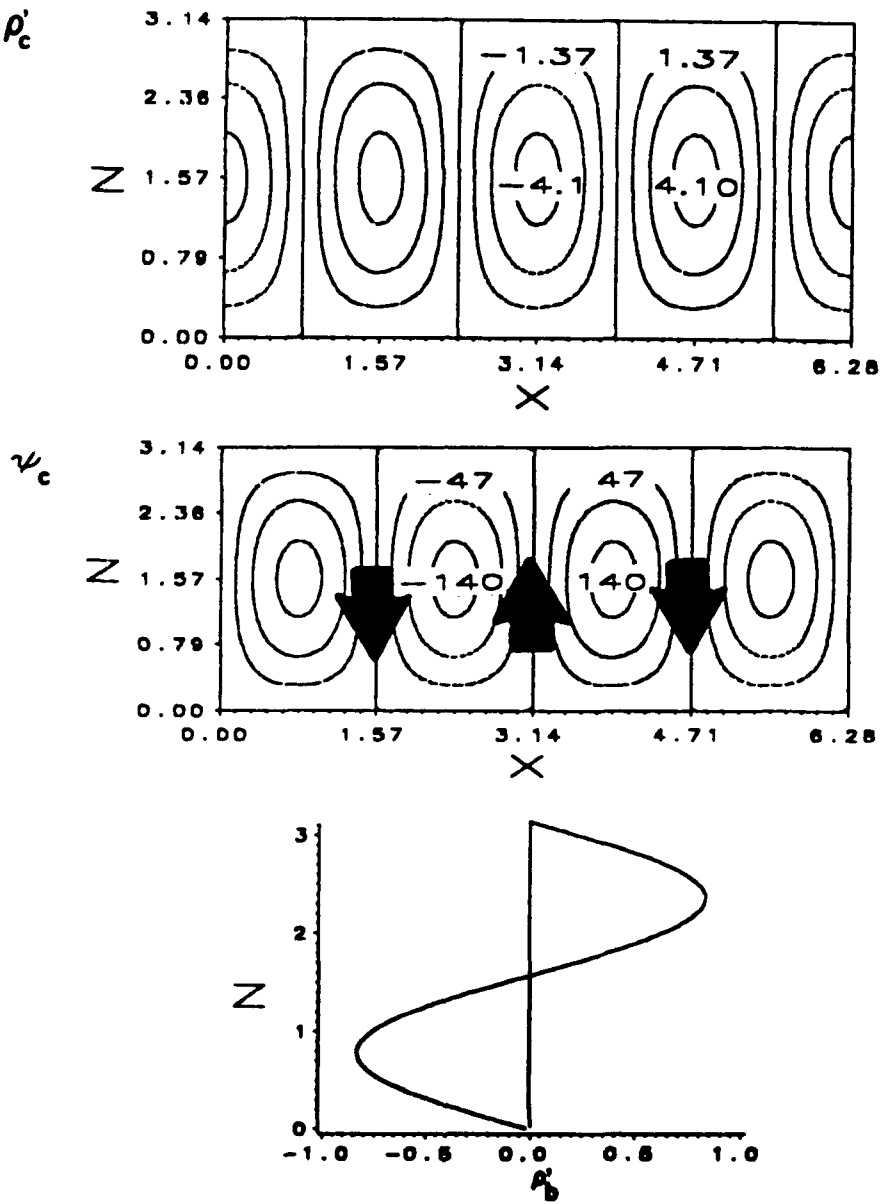


Figure 20 Contours of convective density ρ_c' (kg/m³) and stream function ψ_c' (m²/s), and the modification of the background density ρ_b' (kg/m³) for the steady solution S_m with the values $Ra_S=65$, $Ra_T=65.1$, $K_T=14.286$ m²/s, $\nu=100$ m²/s, $P=7$, $T_{00}=283$ K, $S_{00}=35\%$, $\Delta T=6$ K, $\Delta S=0.742\%$, $m=2$, $j=1$, $g=9.8$ m/s², $a_{mj}=0.493$, and $\tau=0.01$. Here, the circulation is always direct, and the background density is unstable in the interior.

seen in the background density profile (Figure 20).

From the periodic and steady solutions in Figures 19 and 20, we see that if the forcing rates are chosen according to Figure 3, then realistic density perturbations and circulations result. Although no stable toral solutions are found in the region of physically realistic solutions owing to the relationships between the slopes of the diffeo-Hopf and Hopf lines, they may exist for some unphysical values of Ra_S and Ra_T not examined here. The above results and their implications are summarized in the concluding chapter.

Chapter 5

CONCLUSION

Density profile modifications caused by thermohaline convection, which might be observed in estuaries and near melting sea ice, may lead to the trapping of acoustical energy through the development of a near-surface sound channel (Apel, 1987). This channel exists where the density decreases with height, and its boundaries are defined by unstable density gradients in the same way temperature inversions act as boundaries in the atmosphere. In this channel, the competition between the stabilizing salinity gradient and the destabilizing temperature gradient allows steady and periodic solutions, and it is these solutions that modify the background density profiles. We have studied these modifications by examining the existence of Hopf points and their associated periodic solutions. We have also studied the existence of double Hopf points and diffeo-Hopf points as well as their associated toral solutions. Since double Hopf points exist in the partial differential equations representing thermohaline convection, we would expect that toral solutions might cause significant modifications of the background density profiles. However, using a sixteen-coefficient, nonlinear spectral model, we found that these toral solutions are unstable and so do not lead to observable changes in these profiles. Although these *unstable* toral

solutions do not modify the imposed density gradients, they do cause the otherwise unstable periodic solution of wavenumber j to gain stability. We conclude that the presence of a double Hopf point does not always imply the existence of stable toral solutions, while the presence of a diffeo-Hopf point does always imply the existence of a (stable or unstable) toral solution.

In contrast to the values used by Veronis (1968), Knobloch and Proctor (1981), Knobloch et al. (1986), and Huppert and Moore (1976) to study thermohaline convection -- Prandtl number $P = 1$ and ratio of diffusivities $\tau = 0.125$ to 0.5 -- we use the parameter values representing sea water -- $P = 7$ and $\tau = 0.01$. Upon estimating the parameter values characterizing circulations in estuaries, we find that the values of the forcing rates admit only the conductive solution. This result occurs because of the large difference in the values of the solutal and thermal forcing rates: $Ra_S \gg Ra_T$.

However, because $Ra_S \approx Ra_T$ in the melting sea ice case, the rates of forcing produce plausible periodic and steady solutions that significantly modify the background density.

In the periodic regime $Ra_S \approx Ra_T$ of thermohaline convection, the fluid is characterized by a direct circulation for a majority of the period, during which there is an upward transport of lighter fluid.

The fluid is trying to eliminate the unstable density gradient that is caused by the forcing near the boundaries. By attempting to destroy these unstable gradients, the flow creates another unstable gradient in the interior of the fluid. This gradient is produced by an indirect circulation that moves denser fluid upward and lighter fluid downward. Therefore, in a periodic solution, an attempt to destroy an undesirable density gradient creates another. In the periodic case, the size of the sound channel alternately decreases and increases as the unstable density gradient, which does not allow acoustic propagation, alternately moves toward and away from the boundaries. When the interior density gradient is stable, there is an interior sound channel. As this interior gradient becomes unstable, the sound channel separates into two pieces associated with the stable gradients at the boundaries. Thus, the circulation causes the location of the sound channel to fluctuate significantly when the background density is near neutral so that $\tilde{Ra}_S = Ra_T$.

As the forcing rate is increased, the magnitude of the background density modification increases, and so portions of the density profiles become increasingly more unstable. The periodic solution eventually breaks down since it can no longer transport fluid indirectly during an oscillation. In this case, the periodic solutions end abruptly through periodic regular turning points for

all values of the solutal forcing rate Ra_S that were investigated.

The preferred solution is then a steady one, which is a direct circulation. This circulation supports an unstable gradient in the interior of the fluid. Thus, the sound channel is found in two pieces in the steady case, since its boundaries are now the top and bottom of the fluid and those for the interior unstable gradient. In the steady case, there is always a near-surface sound channel.

To study the depth and location of the sound channel, we have investigated periodic and steady solutions. The steady solutions of horizontal wavenumber m and j are found analytically, and the horizontal wavenumber m and j periodic solutions, P_m and P_j , are found numerically, as the thermal forcing rate Ra_T is increased past that for the wavenumber m and j Hopf bifurcation points, H_m and H_j . At $a = a_{mj}$, H_m and H_j coincide to form the double Hopf point H_{mj} . For an aspect ratio $a < a_{mj}$, H_{mj} separates into H_m and H_j , and the P_m solution branches first; for $a > a_{mj}$, P_j branches first. An eigenvalue analysis of the P_m branch, when $a < a_{mj}$, reveals that a harmonic bifurcation occurs for some values of Ra_S , but that no diffeo-Hopf points exist from which toral solutions would emanate from the periodic solution. For values just past that for H_j , the P_j

branch is unstable, but gains stability through a diffeo-Hopf bifurcation D_j . It is this bifurcation that leads to an unstable torus. With the existence of only one diffeo-Hopf point on the unstable periodic solution, there is no stable secondary connecting branch linking the wavenumber m and j periodic branches.

Because of the unstable toral solution, there is no exchange of stability between the horizontal wavenumber m and j periodic solutions, as was found for steady convection by Chang and Shirer (1984) and for rotating convection by Wells and Shirer (1987). All energy put into the catalytic, or wavenumber interaction terms $(m+j, 2)$ and $(m-j, 2)$ dissipates quickly. Also, all energy in the terms having horizontal wavenumber zero and vertical wavenumber four that represent the modification of the background density profile by the toral solution damps to zero. Thus, we are able to represent the modification of the background density field by the $(0, 2)$ terms alone.

As the value of a is varied from that for a_{mj} , the values of the diffeo-Hopf points $Ra_T(D_j)$ and $Ra_T(D_m)$ on the periodic solutions P_j and P_m also vary, and these curves form the boundary of the unstable toral region. With only a D_j bifurcation point on the unstable P_j solution for $a < a_{mj}$ and a D_m point on the unstable solution P_m for a

$> a_{mj}$, we have only a single diffeo-Hopf line on each side of a_{mj} .

The diffeo-Hopf point is always on the second periodic branch, so that $Ra_T(H_m) < Ra_T(H_j) < Ra_T(D_j)$ for $a < a_{mj}$, and $Ra_T(H_j) < Ra_T(H_m) < Ra_T(D_m)$ for $a > a_{mj}$, and so there is always an unstable toral solution. Therefore, by knowing the relationships between the Hopf and diffeo-Hopf lines, we can determine whether the bifurcating quasi-periodic solution is stable or unstable.

In rotating convection, where D_m and D_j both existed on one side of the double Hopf point so that $Ra_T(H_m) < Ra_T(D_m) < Ra_T(H_j) < Ra_T(D_j)$ (Wells and Shirer, 1987), stable toral solutions were found.

The truncation chosen in the present sixteen-coefficient model is similar to that used by both Chang and Shirer (1984) and Wells and Shirer (1987), whose models successfully captured the observed transfer of energy from larger to smaller horizontal wavenumbers.

The relationships between the diffeo-Hopf curves, which bound the toral region, and the Hopf curves can be approximated using a power series analysis of the partial differential equations. This analysis, which is still being developed, will also provide the truncation level required for modeling toral solutions and the relative importance of each component of the truncation in the representation of these toral solutions. With this analysis, we will

be able to see whether the trigonometric representation of the variables in the present model is sufficient, and how sensitive the existence and stability of the toral solution are to the number of terms included in the expansion.

REFERENCES

Apel, J.R., 1987: Principles of Ocean Physics. Academic Press, 634 pp.

Baines, P.G. and A.E. Gill, 1969: On thermohaline convection with linear gradients. J. Fluid Mech., 37, 289-306.

Chang, H.R. and H.N. Shirer, 1984: Transitions in shallow convection: An explanation for lateral cell expansion. J. Atmos. Sci., 41, 2334-2346.

Da Costa, L.N., E. Knobloch and N.O. Weiss, 1981: Oscillations in double-diffusive convection. J. Fluid Mech., 109, 25-43.

Dyer, K.R., 1973: Estuaries: A Physical Introduction. John Wiley and Sons, 140 pp.

Feldstein, S.B., 1987: Bifurcation analysis of periodic solutions. Chapter 14 in Nonlinear Hydrodynamic Modeling: A Mathematical Introduction, pp. 355-383, H.N. Shirer (Ed.). Lecture Notes in Physics, 271, Springer-Verlag, Heidelberg.

Guckenheimer, J. and P. Holmes, 1983: Nonlinear Oscillations, Dynamical Systems, and Bifurcations of Vector Fields. Applied Mathematical Sciences, 42, Springer-Verlag, New York, 453 pp.

Higgins, R.W., 1987: From the equations of motion to spectral models. Chapter 3 in Nonlinear Hydrodynamic Modeling: A Mathematical Introduction, pp. 47-69, H.N. Shirer (Ed.). Lecture Notes in Physics, 271, Springer-Verlag, Heidelberg.

Hirschberg, P.A., 1987: Hierarchies of transitions: Secondary branching. Chapter 9 in Nonlinear Hydrodynamic Modeling: A Mathematical Introduction, pp. 197-224, H.N. Shirer (Ed.). Lecture Notes in Physics, 271, Springer-Verlag, Heidelberg.

Huppert, H.E. and D.R. Moore, 1976: Nonlinear double-diffusive convection. J. Fluid Mech., 78, 821-854.

Iooss, G. and D.D. Joseph, 1980: Elementary Stability and Bifurcation Theory. Springer-Verlag, New York, 286 pp.

Knobloch, E., D.R. Moore, J. Toomre and N.O. Weiss, 1986: Transitions to chaos in two-dimensional double-diffusive convection. J. Fluid Mech., 166, 409-448.

Knobloch, E. and M.R.E. Proctor, 1981: Nonlinear periodic convection in double-diffusive systems. J. Fluid Mech., 108, 291-316.

Laufersweiler, M.J., 1987: The expected branching solution: Preferred wavelengths. Chapter 7 in Nonlinear Hydrodynamic Modeling: A Mathematical Introduction, pp. 131-163, H.N. Shirer (Ed.). Lecture Notes in Physics, 271, Springer-Verlag, Heidelberg.

Nese, J.M., 1987: The transition to turbulence. Chapter 15 in Nonlinear Hydrodynamic Modeling: A Mathematical Introduction, pp. 384-411, H.N. Shirer (Ed.). Lecture Notes in Physics, 271, Springer-Verlag, Heidelberg.

Nese, J.M., 1989: Quantifying local predictability in phase space. Physica D, 35, 237-250.

Pyle, R.J., 1986: On modal truncations for branching temporally periodic solutions. MS Thesis, Department of Meteorology, The Pennsylvania State University, University Park, PA, 109 pp.

Ruelle, D., 1989: Elements of Differential Dynamics and Bifurcation Theory, Academic Press, 187 pp.

Sparrow, C., 1982: The Lorenz Equations: Bifurcations, Chaos, and Strange Attractors. Applied Mathematical Sciences, 41, Springer-Verlag, Heidelberg, 269 pp.

Turner, J.S., 1973: Double-diffusive convection. Chapter 8 in Buoyancy Effects in Fluids, pp. 251-287, Cambridge University Press, London and New York.

Veronis, G., 1965: On finite amplitude instability in thermohaline convection. J. Mar. Res., 23, 1-17.

Veronis, G., 1968: Effect of a stabilizing gradient of solute on thermal convection. J. Fluid Mech., 34, 315-336.

Wells, R. and H.N. Shirer, 1987: Bifurcation from steady to toral solutions in fluid flow models. In Bifurcation Phenomena in Thermal Processes and Convection, pp. 11-21, H.H. Bau, L.A. Bertram, and S.A. Korpela (Eds.). American Society of Mechanical Engineers, New York.